Journal Pre-proof

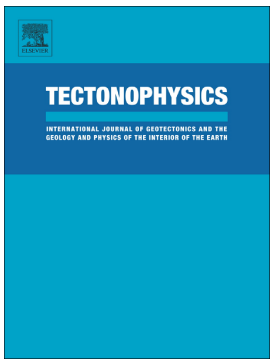

Pre-existing basement faults controlling deformation in the Jura Mountains fold-and-thrust belt: Insights from analogue models

Marc Schori, Frank Zwaan, Guido Schreurs, Jon Mosar

PII: S0040-1951(21)00262-6

DOI: https://doi.org/10.1016/j.tecto.2021.228980

Reference: TECTO 228980

To appear in: *Tectonophysics*

Received date: 17 November 2020

Revised date: 28 May 2021

Accepted date: 19 June 2021

Please cite this article as: M. Schori, F. Zwaan, G. Schreurs, et al., Pre-existing basement faults controlling deformation in the Jura Mountains fold-and-thrust belt: Insights from analogue models, *Tectonophysics* (2018), https://doi.org/10.1016/j.tecto.2021.228980

Pre-existing basement faults controlling deformation in the Jura Mountains fold-and-thrust belt: insights from analogue models

Marc Schori[1*], Frank Zwaan[2], Guido Schreurs[2], Jon Mosar[1]

(1) Earth Sciences, University of Fribourg, Chemin du Musée 6, CH-1700 Fribourg, Switzerland, (2) Institute of Geological Sciences, University of Bern, Baltzerstrasse 3, CH-3012 Bern, Switzerland, * marc.schori@unifr.ch

Abstract

Pre-existing faults in the mechanical basement are believed to play an important role in controlling deformation of the thin-skinned Jura Mountains fold-and-thrust belt, which constitutes the northernmost extension of the European Alps. We use brittle-viscous analogue models to investigate the influence of frontal and oblique basement steps on the subsequent evolution of structures during thin-skinned shortening. Vertical offset between two rigid baseplates (simulating the mechanical basement) causes the formation of reverse faults and grabens in the overlying brittle layers that are not reactivated during subsequent thin-skinned shortening. However, baseplate steps localise deformation, causing a temporary frontward propagation of deformation in an early stage and inhibiting propagation afterwards. Downward baseplate steps induce very strong deformation localisation and foster the formation of fault-bend folds. Models featuring upward steps develop step-controlled pop-up structures with imbricated fronts and viscous ramps that shorten dynamically with progressive contraction. We find that deformation localisation increases both with higher step-throws and lower obliquity (α) of the strike of the step (e.g. frontal step α = 0°). With increasing step-throws, α = 30° and α = 45° oblique upward-steps lead to a characteristic imbrication of the brittle cover with laterally confined thrust-slices and step-parallel oblique-thrusts, which rotate up to 15° about a vertical axis over time. Step-controlled backthrusts preceding the formation of thrust-slices do not show notable rotation and hence constitute excellent indicators for the orientation of oblique upward-steps. The topographic patterns of oblique-step models resemble individual thin-skinned structures of the Internal Jura (i.e. Pontarlier and Vuache fault zones, the nappe system SE of Oyonnax and the Chasseral anticline), strongly suggesting that pre-existing NNE-SSW and NW-SE striking oblique upward-steps in the basement controlled deformation in the overlying cover. Our model results may be applied to other thin-skinned fold-and-thrust belts worldwide that formed above pre-existing basement structures.

Keywords

Jura Mountains fold-and-thrust belt; analogue modelling; lineament; oblique ramp; basement-cover interaction; localization of deformation at basement fault

1 Introduction

The Jura Mountains fold-and-thrust belt (JFTB) forms the outermost front of the Central and Western European Alps that became detached in Triassic evaporites during Middle Miocene (Serravallian) to Pliocene times (Buxtorf, 1907; Laubscher, 1961). The thin-skinned JFTB evolved above a pre-structured basement, which affected the deformation style of the Mesozoic and Cenozoic sedimentary cover (Homberg et al., 2002; Laubscher, 1986, 1961; Malz et al., 2019; Philippe et al., 1996; Tschanz, 1990). Pre-existing basement structures frequently controlled the formation of cover structures that are oblique to the JFTB transport directions (Laubscher, 1961). Although obscuring most underlying basement structures, the JFTB is full of inherited strike directions, which highly motivated us to study the formation of complex fold and thrust arrangements.

The aim of this study is to understand the kinematic and mechanic conditions of basement-controlled structures in the detached cover of the JFTB. First, we present brittle-viscous sandbox analogue-models that explore the spatial and kinematic evolution of a brittle sand cover above a viscous detachment, migrating across oblique and frontal basement steps associated with the reactivation of inherited faults. Thereafter we compare structures observed in our analogue models with natural examples from the JFTB. Although we study the case of the thin-skinned JFTB in the first place, our model results may be applied to other fold-and-thrust belts worldwide that deformed above pre-existing basement structures. Some examples amongst others, where inherited structures are proposed to have exerted an important structural control, are the Taiwan orogen (Yang et al., 2006, 1996), the Apennines (Coward et al., 1999; Tavarnelli, 1997), the Zagros Mountains (Berberian, 1995) and the Prebaetic System of the Baetic Cordillera in Spain (Peper and Cloetingh, 1992).

2 Regional setting

2.1 Jura Mountains fold-and-thrust belt

The Jura Mountains are an arc-shaped mountain range of ~300 km width and a transect length of ~75 km at its centre (Fig. 1a). The Mesozoic and Cenozoic cover of the Jura Mountains and the western Molasse Basin (Fig. 1a, b) was detached in Triassic evaporites and transported north-westwards, which was proposed by Buxtorf (1907, 1916) and Schardt (1908) based on observations in railway tunnels and because no rocks exposed in the JFTB pre-date a Triassic age. Several decades later, boreholes and seismic lines within the detached Molasse Basin and the Jura Mountains confirmed the existence of a regional basal décollement in Triassic evaporites (Burkhard, 1990; Jordan, 1992; Jordan and Nuesch, 1989; Laubscher, 1961; Lienhardt, 1962; Michel et al., 1953; Sommaruga, 1997). The basal detachment of the JFTB is very probably connected with the Alpine sole thrust in the south-east, that roots beneath the External Crystalline Massifs (ECMs) of the Alps (Burkhard, 1990; Bellahsen et al., 2014, Fig. 1b), namely the Belledonne, Aiguilles-Rouges, Mont-Blanc, Aar and Gotthard Massifs (Fig. 1a). Therefore, the evolution of the JFTB and the exhumation of the ECMs were coupled and contemporaneous (Becker, 2000; Burkhard, 1990; Laubscher, 1986). From structural relations of Tertiary sediments across the Jura Mountains, the main folding and thrusting of the JFTB occurred between about 12 and 4 Ma (Becker, 2000 and references therein), which we consider the thin-skinned main formation stage of the JFTB. However, the basal décollement of the

JFTB and Molasse Basin was active before (Deville et al., 1994; Leloup et al., 2005; Looser et al., 2020). From the thermal and structural evolution of the ECMs, Leloup et al. (2005) concludes that the Alpine sole thrust (see Fig. 1b) prolonged into the Triassic evaporites beneath the Molasse Basin by ~15 Ma at the latest. This is supported by recent U-Pb dating of calcite veins in the Schafisheim-1 borehole situated in the Molasse Basin west of Zürich (see position in Fig. 1a) that shows activity of the basal décollement at 14.3 ± 0.5 Ma (Looser et al., 2020).

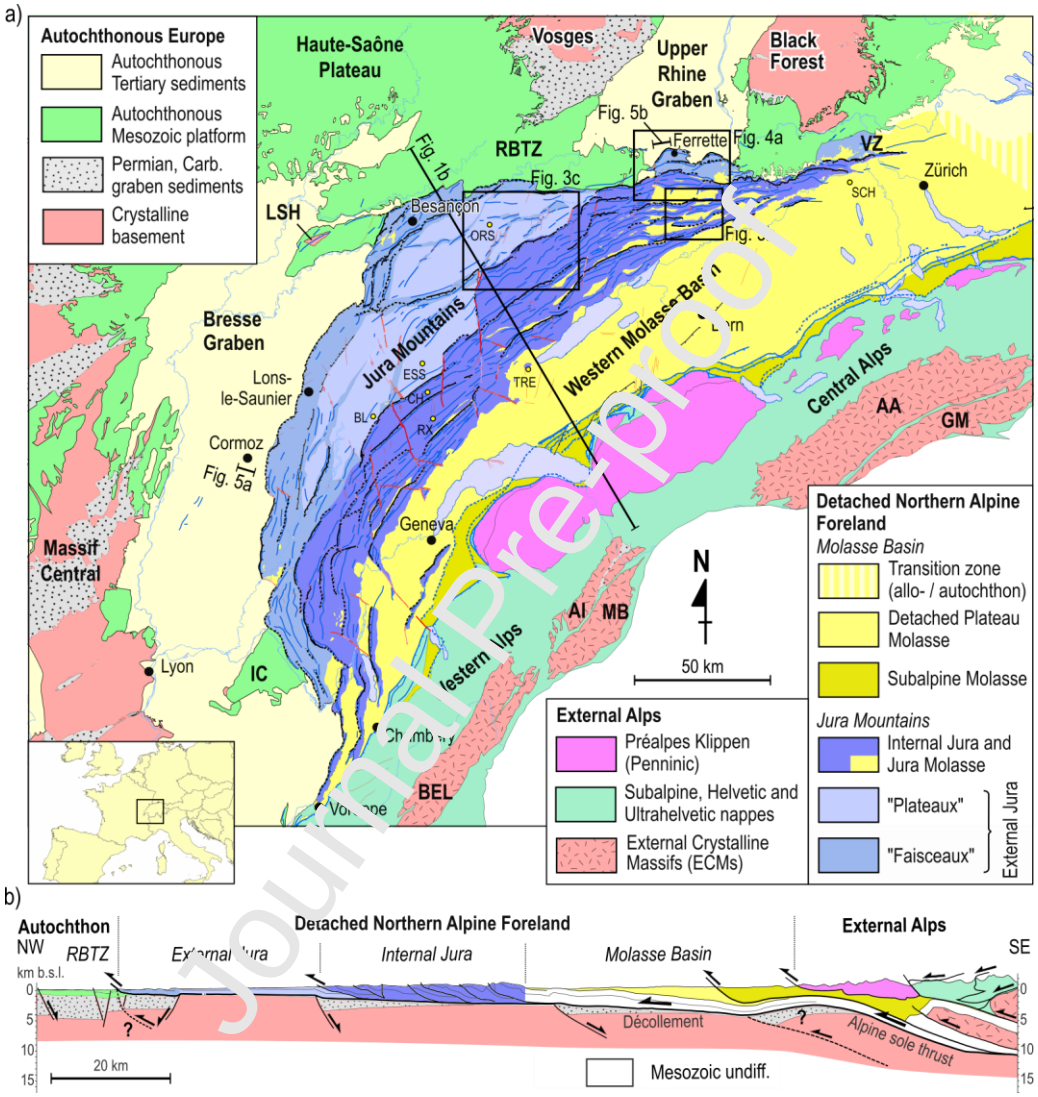

Fig. 1 a) Tectonic map of the Jura Mountains and surroundings, based on existing maps (Chauve and Perriaux, 1974; Sommaruga et al., 2017; Trümpy, 1980) and new observations. b) Regional cross-section modified from Sommaruga et al. (2017). AA: Aar Massif, AI: Aiguilles Rouges Massif, BEL: Belledonne Massif, GM: Gotthard Massif, IC: Ile Crémieu, LSH: La Serre Horst, MB: Mont Blanc Massif, RBTZ: Rhine-Bresse Transfer Zone, VZ: Vorfaltenzone. Indicated boreholes are BL: Bonlieu-1, CH: Châtelblanc-1, ESS: Essavilly-101, ORS: Orsans-1, RX: Risoux-1, SCH: Schafisheim-1 and TRE: Treycovagnes-1.

The JFTB is classically divided into a highly deformed internal tectonic domain and a considerable less deformed external part (Chauve and Perriaux, 1974; Trümpy, 1980, Fig. 1a). The strongly deformed Internal Jura or High Jura (Fig. 1) shows maximum northwest displacements of about 30 km (Affolter, 2004; Laubscher, 1965; Philippe et al., 1996), featuring well-developed ramps and fault-propagation

folds that partially led to kilometric duplication of the Mesozoic cover (Fig. 1b, Winnock, 1961; Aubert, 1971; Sommaruga, 1997). The less deformed External Jura is subdivided into narrow zones of localised deformation called “faisceaux” (meaning “bundles” in English) and scarcely folded and intact plateaus (Fig. 1a). These plateaus are blocks of Mesozoic carbonates, each several hundred square kilometres large, embedded within the faisceaux (Fig. 1a).

The front of the JFTB is controlled by rift segments of the European Cenozoic Rift System (ECRIS, Dèzes et al., 2004; Lacombe and Bellahsen, 2016; Madritsch et al., 2008; Malz et al., 2016; Ustaszewski and Schmid, 2006; Ziegler, 1992), i.e. the Bresse Graben (BG) to the west and the Upper Rhine Graben (URG) to the north, connected by the Rhine-Bresse Transfer Zone (RBTZ, Fig. 1a). Therefore, faisceaux at the front of the JFTB follow extensional structures of the ECRIS (Bièvre and Mercier, 2010; Chauve and Perriaux, 1974; Glangeaud, 1951; Lienhardt, 1962; Martin and Mercier, 1996; Michel et al., 1953; Philippe et al., 1996).

2.2 Mechanical stratigraphy

The mechanical basement of the JFTB (footwall) encompasses the geological units beneath the basal décollement in Triassic evaporites. Apart from the crystalline basement, this includes Permian and Carboniferous continental sediments deposited within troughs in the crystalline basement as well as the Triassic series beneath the basal décollement (Fig. 2). The evaporite décollement of the JFTB concentrated predominantly in halite-bearing layers (Deville, 2021; Sommaruga et al., 2017), deposited in shallow basins on an epicontinental platform (Lienhardt et al., 1984; Philippe et al., 1996). Salt occurs mainly in Upper Triassic evaporites (Keuper group) in the Central and Southern Jura and mostly in Middle Triassic series (Muschelkalk group) in the Eastern Jura (Debrand-Passard et al., 1984; Guellec et al., 1990; Jordan, 1992; Laubscher, 1986, 1961; Philippe et al., 1996; Sommaruga et al., 2017).

The stratigraphy in Fig. 2 is representative of the Central Jura, where the décollement is localised in Upper Triassic evaporites (Laubscher, 1961; Philippe et al., 1996). We estimate a décollement/cover thickness ratio of about 1/8, assuming the Upper Triassic salt system to be the basal décollement (Fig. 2). However, anhydrite layers present throughout the Triassic series were at least partially involved in the décollement (Jordan, 1992; Müller et al., 1981), leading to a décollement/cover thickness ratio of ca. 1/5 (Fig. 2). This ratio increases even more towards the front of the JFTB, where the detached Mesozoic cover is extensively eroded due to Eocene to Oligocene rift-shoulder uplift associated with the formation of the ECRIS (Illies, 1972; Michon, 2000) and forebulging of the peripheral Alpine foreland basin (Burkhard and Sommaruga, 1998; Laubscher, 1992). Although detachments in the overlying Jurassic and Cretaceous series can occur locally (Malz et al., 2019; Noack, 1995; Nussbaum et al., 2017; Philippe et al., 1996; Schori et al., 2015, see Fig. 2), we focus on the role of the main basal Triassic décollement in this study.

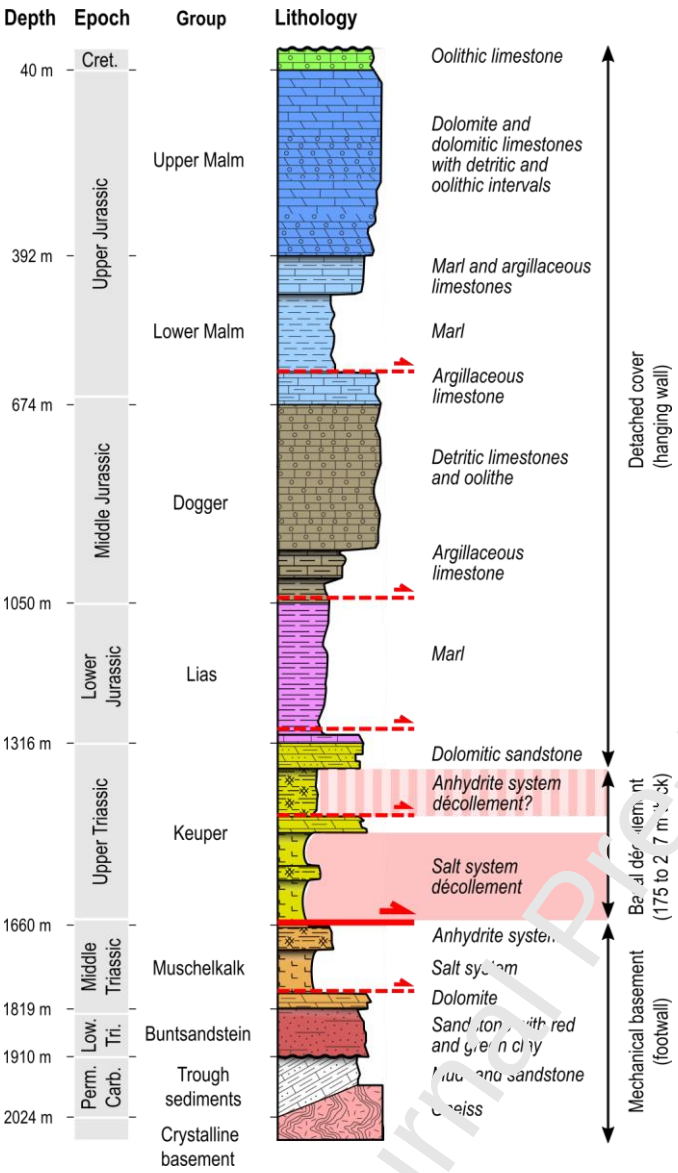

Fig. 2 Representative stratigraphy of the Central Jura Mountains based on borehole Essavilly-101 (Delmas, 1965). The top of the mechanical basement of the JFTB (footwall) lies near the bottom of the Upper Triassic series. The Upper Triassic anhydrite system at least partially contributed to the basal décollement zone, next to the Upper Triassic salt system. Note that local upper detachments occur in the Jurassic series.

2.3 Inherited basement faults

In the URG and Vorfaltenzone (Fig. 1a), numerous studies of seismic lines, boreholes and gravimetry provide well-constrained insights into faults affecting the basement, with structural orientations being frequently associated with the Variscan orogeny and post-Variscan collapse (Egli et al., 2016; Hauber, 1993; Illies, 1972; Larroque and Laurent, 1988; Laubscher, 1982; Madritsch et al., 2018, 2009, 2008; Madritsch and Deplazes, 2014; Philippe, 1995; Rat, 1974; Rotstein et al., 2005; Ustaszewski, 2004). There are three main Palaeozoic trends present (Illies, 1962; Reisdorf and Wetzel, 2018; Schumacher, 2002), which originate from NNE-SSW (“Rhenish”, N010°-N020°) striking Variscan sinistral shear zones, NW-SE (“Hercynian”, N120°-N130°) striking Variscan dextral shear zones and ENE-WSW (“Erzgebirgian”, N070°-N080°) striking Variscan dislocation zones (Fig. 3a). Some of these Palaeozoic fault zones were transpressionally or transtensionally reactivated during the Mesozoic opening of the

Alpine Tethys, as well as during the evolution of the ECRIS and the Alpine flexural foreland basin system in Cenozoic times (Illies, 1962; Laubscher, 1986; Madritsch et al., 2009; Meier, 2010; Reisdorf and Wetzel, 2018; Schumacher, 2002; Wetzel et al., 2003; Ziegler, 1988a; Ziegler and Dèzes, 2007). This led to: (1) depositional differences of Mesozoic and Cenozoic sediments along fault zones, (2) mechanical heterogeneities in the deformed sedimentary cover and (3) substantial vertical offsets of the basement and the cover. In this paper, we test the influence of the latter two predispositions on the evolution of the JFTB.

2.4 Lineaments in the Jura Mountains

In the Eastern Jura, folds frequently deviate from ideal cylindrical geometries, being bow-shaped, sigmoidal shaped or simply oblique to the transport direction of the JFTB in map view (Allenbach and Wetzel, 2006; Laubscher, 2008a; Meier, 2010). Such anomalous fold axes connect to lineaments with a rough NNE-SSW (Rhenish) orientation (Fig. 3a, b). The existence and implications of Rhenish lineaments in the Eastern Jura have been debated for more than a century (Laubscher, 2008a; Steinmann, 1892). Nowadays, anomalous fold orientations in the Eastern Jura are interpreted as thin-skinned structures pre-conditioned by NNE-SSW striking normal faults in the basement, that are southward continuations of Eo-Oligocene URG faults (Allenbach and Wetzel, 2006; Boigk and Schöneich, 1974; Laubscher, 2008a, 2008b; Meier, 2010; Steinmann, 1902), forming preferentially along Palaeozoic Rhenish structural trends.

Also in the central External Jura, the Mesozoic cover deformed along lineaments (see Fig. 3c), which are oblique to the general northwest-directed tectonic transport of the JFTB. In Fig. 3c, lineaments strike NE-SW, NNE-SSW (Rhenish) and ENE-WSW (Erzgebirgian). Along these lineaments, we observe alignments of short, dissected folds (Fig. 3c). Analogous to the situation in the Eastern Jura (Fig. 3b), we propose that lineaments in Fig. 3c are the consequence of aforementioned pre-existing basement steps, which controlled deformation of the detached cover during formation of the JFTB.

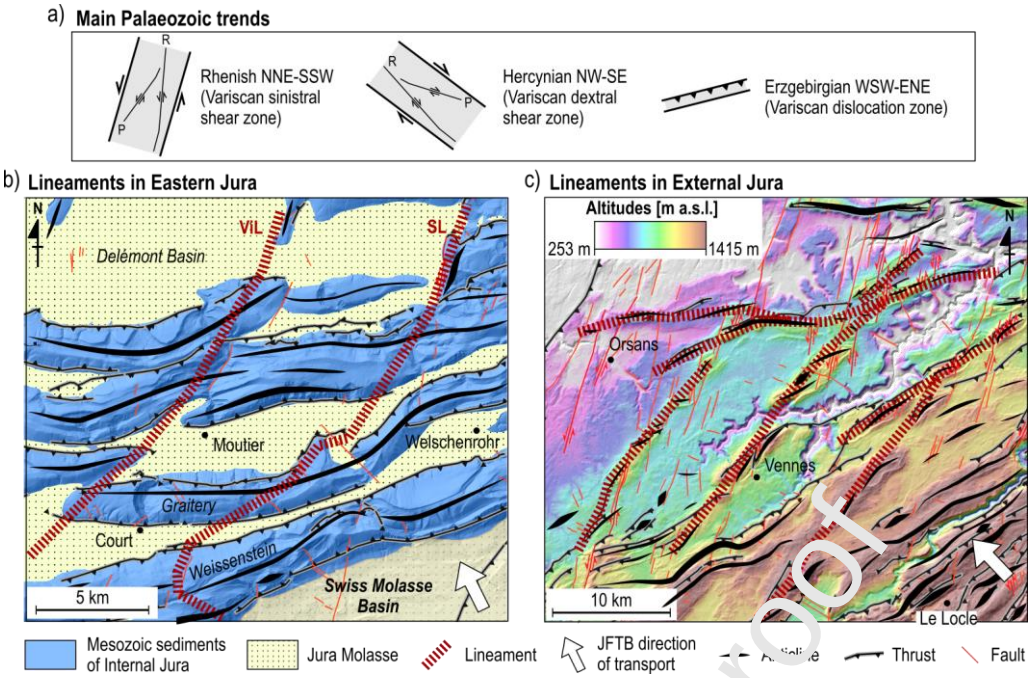

Fig. 3 Examples of lineaments in the JFTB. See overview map (Fig. 1a) for locations. a) Scheme of main Palaeozoic trends in the area of the URG, illustrating strike variations due to Riedel shear structures (R and P) for shear zones. b) Folds in the Eastern Jura tend to be bow-shaped, laterally confined or reveal a sigmoidal geometry (e.g. Graitery Anticline). Lineaments with a NNE Rhenish orientation were proposed for this region (Allenbach and Wetzel, 2006; Laubscher, 2008b; Meier, 2010; Steinmann, 1902). The Schwarzwald Line (SL) and Vicques Line (ViL) are drawn according to Laubscher (2008b). c) Area in the External Jura showing lineaments composed of short, dissected folds that align along connected topographical elevations. JFTB transport directions are after Philippe et al. (1996). Note that lineaments are oblique to the local JFTB transport direction.

3 Examples of basement-fault related structures

3.1 Basement-fault controlled frontal faisceau

The Ferrette Zone is a faisceau at the front of the Eastern Jura (see Fig. 1a for location). Thrusts at the front of the Ferrette Zone strike NNE-SSW and abruptly turn into a rough E-W direction (Fig. 4a). Structural analysis (Ustaszewski and Schmid, 2006 and references therein) reveals two intersecting fault systems in the basement, which are oriented NNE-SSW and E-W (Fig. 4a). Both systems formed during Eo-Oligocene rifting related to the formation of the URG and provided downward steps during formation of the JFTB, localising deformation in the Mesozoic cover (Fig. 4b). Note that downward steps in the Pre-Mesozoic basement controlled the formation of the two anticlines in Fig. 4b.

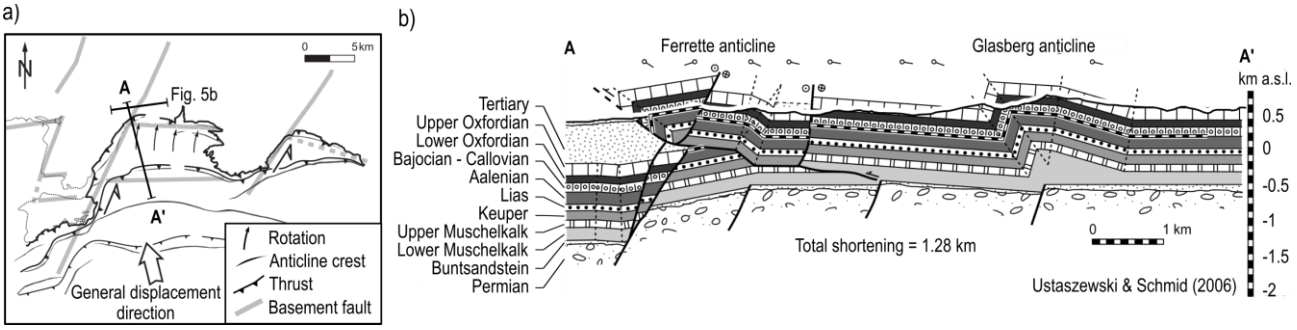

Fig. 4 Structural overview of the Ferrette Zone. a) Structural overview sketch, indicating the relation between NNE-SSW and E-W striking basement faults and thin-skinned structures (Ustaszewski and Schmid, 2006). See Fig. 1a for location. b) Cross-section across the Ferrette Zone (Ustaszewski and Schmid, 2006).

3.2 Basement-fault induced cover structures

To the west of the JFTB, in the autochthonous Bresse Graben close to Cormoz (Fig. 1a), Bergerat et al. (1989) interpreted an ECORS seismic line, showing a relatively steep normal fault of 75° in the crystalline basement, above which a reverse fault disrupts the Mesozoic cover (Fig. 5a). There is also a minor extensional collapse in the Jurassic series, above the higher western basement block. The Triassic salt system accommodates offsets in the basement (Fig. 5a). Normal faults in the basement that induce reverse faults in the cover are also documented in the URG (Ustaszewski et al., 2005), north of Ferrette (Fig. 5b, for location see Fig. 1a). Note that the cross-sections in Fig. 5 show extensional systems in connection with graben formation of the ECRIS, but the dominant structures in the Mesozoic cover are reverse faults (Fig. 5). We also like to point out that basement faults in Fig. 5a do not continue as a single fault into the cover. The salts in Fig. 5a distribute basement induced deformation, i.e. decoupling (e.g. Withjack and Callaway, 2000), causing different structures in the cover than in the basement.

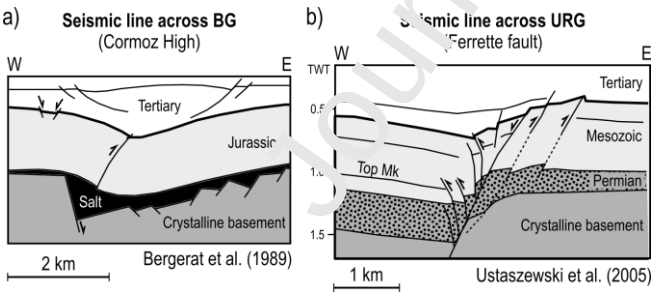

Fig. 5 Basement induced structures in the Bresse Graben (BG) and Upper Rhine Graben (URG). a) Seismic line interpretation across the Cormoz High in the BG, adapted from Bergerat et al. (1989). b) Seismic line interpretation across the URG, adapted from Ustaszewski et al. (2005). Profile traces are indicated in the tectonic overview map in Fig. 1a.

4 Working hypothesis

Our working hypothesis states that during JFTB formation, deformation of the Mesozoic cover was influenced by offsets along pre-existing basement faults resulting in thrust ramps. Since basement faults were inherited, they were usually oblique to the JFTB transport direction and a variety of oblique, lateral and frontal ramps resulted from the interaction of the cover with basement faults (Fig. 6a). Furthermore, depending on the relative vertical offset of basement faults, the décollement had to ramp

upwards (Fig. 6b) or downwards (Fig. 6c) to compensate for higher or lower basement positions respectively.

In order to test the influence of basement faults on the structures in the JFTB, we performed a series of analogue model experiments, in particular testing different throws and strikes of basement faults.

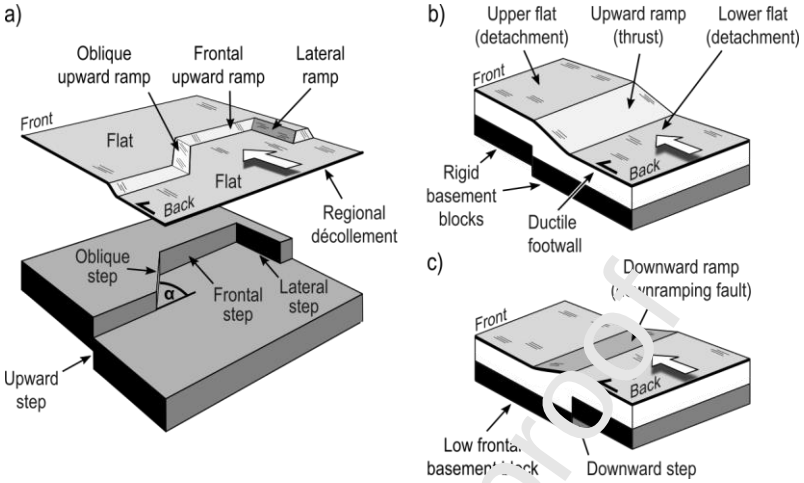

Fig. 6 Sketches illustrating different ramp types of a regional décollement above pre-existing vertical steps in the basement. a) Schematic drawing showing different types of upward ramps (after Capotria et al., 1992) above corresponding basement steps. The angle α specifies the angular deviation of an oblique step from a frontal step and therefore, the angle α is 0° for a frontal step and 90° for a lateral step. Transport directions are indicated with white arrows. b) A low-angle thrust-ramp accommodates a vertical upward step. c) A frontal downward ramp covers a vertical downward step in the basement.

5 Material and methods

5.1 Material properties in analogue models

We apply a 1:20,000 model-to-nature scaling ratio for our brittle-viscous models, so that 70 mm thick dry quartz sand simulates ca. 1400 m of uniform brittle Mesozoic cover. One model tested a reduced cover of 40 mm (corresponding to 800 m in nature). The sand has a homogeneous density (ρ) of ca. 1560 kg/m^3 when sieved from 30 cm height (Klinkmüller et al., 2016), its grain size (ø) ranges between 60-250 µm and its angle of internal friction is 36.1° (Zwaan et al., 2016, 2018a, see Table 1). The sand surface is flattened with a scraper at every centimetre during model preparation. One model is scanned using X-Ray Computed Tomography (CT), for which we create a layering visible on CT-imagery by adding a very thin corundum layer (< 1 mm) on top of the sand pack after each scraping. The corundum sand has a density (ρ) of 1890 kg/ m^3, grain sizes (ø) between 88-125 µm and an angle of internal friction of 37° (Panien et al., 2006). A viscous layer of about 13 mm thickness represents a 260 m thick basal décollement zone of weak Triassic salt layers (Fig. 2). The viscous material consists of Polydimethylsiloxane (PDMS, type Dow Corning SGM-36) and corundum sand, mixed in a one-to-one weight ratio. The mixture density (ρ) is ca. 1600 kg/m^3, close to the density of the quartz sand (Table 1), and has a near-Newtonian rheology with a viscosity (η) of $1.5 \cdot 10^5$ Pa·s given our model strain rates (Zwaan et al., 2018b). This way, the density profiles of the models correspond to conditions in the Jura Mountains, where Upper Triassic salt systems are usually associated with various contents of clay, anhydrite and gypsum, and relatively dense compared to

pure halite (Bergerat et al., 1990, see Table 2). The density profile of our models also prevents diapirism, taking account of the general absence of salt diapirs in the JFTB.

Table 1 Material properties after Panien et al. (2006) and Zwaan et al. (2016, 2018a, b).

Granular materials	**Quartz sand**	**Corundum sand**
Grain size range (ø)	60-250 µm	88-175 µm
Bulk density (sieved, ρ)	1560 kg/m^3	1890 kg/m^3
Angle of internal friction	36.1°	37°
Angle of dynamic-stable friction	31.4°	32°
Cohesion (C)	9 ± 98 Pa	39 ± 10 Pa
Viscous material	**PDMS/corundum-sand mixture**	
Weight ratio PDMS/corundum	1/1	
Mixture density (ρ)	Ca. 1600 kg/m^3	
Viscosity (η)*	Ca. 1.5·10^5 Pa·s	
Rheology (with sensitivity to strain)	Near-Newtonian (n = 1.05 to 1.10)	

* Valid for model strain rates < 10^{-4} s^{-1}

5.2 Model scaling

Analogue models are scaled with the equation $\sigma^* = \rho^* g^* L^*$ (Eq. 1, Hubbert, 1937; Ramberg, 1981) where σ^*, ρ^*, g^* and L^* represent the ratios of stress, density, gravity and length between the model and the natural example. The gravity ratio is $g^* = 1$ and the density ratio ρ^* corresponds to ca. 0.6 (Table 2), so that $\sigma^* = 0.6L^*$, where L^* is set to 1/20,000. The viscometric function $\sigma^* = \eta^* \dot{\varepsilon}^*$ (Eq. 2, Weijermars and Schmeling, 1986) is used to calculate the strain rate ratio ($\dot{\varepsilon}^*$), where η^* is the viscosity ratio and the equation $\dot{\varepsilon}^* = v^*/L^*$ (Eq. 3) provides the velocity ratio (v^*).

In nature, the viscosity of pure dry halite is around 10^{18} Pa·s, whereas the effective viscosity of halite with small grain sizes at high temperatures is 10^{17} Pa·s, ranging up to 10^{20} Pa·s for large grain sizes at low temperatures (van Keken et al., 1993). Present-day maximum overburden of the basal décollement level in the Jura Mountains hardly exceeds 2.3 km (e.g. borehole Treycovagnes-1 in Sommaruga, 1997; Sommaruga et al., 2012), which at a temperature gradient of 35°C / km calculates to relatively low maximum temperatures of about 80°C. In addition, the Triassic salt systems of the Jura Mountains commonly contain various amounts of clay, anhydrite and gypsum, which further increases the viscosity of the salt. We therefore aim to simulate a rock salt décollement with an elevated viscosity (> 10^{18} Pa·s).

The maximum displacement of the central Jura Mountains is about 30 km (Affolter, 2004; Laubscher, 1965; Philippe et al., 1996). Since the main Jura formation stage lasted roughly 8 Ma (Becker, 2000), we estimate an average natural displacement velocity of 3.75 mm per year. We adjust the model velocity accordingly to 10 cm/h to obtain a velocity ratio (v^*) of 2.34·10^5 (Table 2). This translates to a strain rate ratio ($\dot{\varepsilon}^*$, see Eq. 3) of 4.67·10^9, which in turn yields an appropriately high viscosity (η) of 2.34·10^{19} Pa·s for the simulated salt system (Eq. 2). The time ratio is calculated with $t^* = 1/\dot{\varepsilon}^*$ so that one model hour corresponds to 533 kyr in nature (Table 2).

Table 2 Parameters used for model scaling. Densities for the Jura Mountains are deduced from density logs of boreholes Bonlieu-1 and Châtelblanc-1 (Bergerat et al., 1990, see positions in Fig. 1a). The densities given for the décollement (ρ_d) and cover (ρ_c) in the Jura correspond to densities of the Upper Triassic salt system and Jurassic limestone-marl layers, respectively..

Parameter	Model	Jura Mountains	Ratio
Density of décollement (ρ_d)	1600 kg/m^3	2500 kg/m^3	0.6
Density of cover (ρ_c)	1560 kg/m^3	2530 kg/m^3	0.6
Gravitational acc. (g)	9.81 m/s^2	9.81 m/s^2	1
Length (L)	1 cm	200 m	$5 \cdot 10^{-5}$
Velocity (v)	10 cm/h	3.75 mm/yr	$2.34 \cdot 10^{5}$
Strain rate ($\dot{\varepsilon}$)			$4.67 \cdot 10^{9}$
Stress (σ)			$3 \cdot 10^{-5}$
Viscosity (η)	ca. $1.5 \cdot 10^{5}$ Pa·s	$2.34 \cdot 10^{19}$ Pa·s	$6.42 \cdot 10^{-15}$
Time (t)	1 h	533 kyr	$2.14 \cdot 10^{-10}$

5.3 Experimental set-up

The experimental apparatus is 117 cm long for frontal step experiments and 113 cm long for oblique steps and flat-base models, at a constant width of 50 cm (Fig. 7a). The sandbox frame consists of 2.1 cm thick rigid pine-plywood with two mobile parts: a horizontal mobile frontal baseplate and a vertical mobile backstop (Fig. 7b). The bottom of the apparatus includes two baseplates (Fig. 7a, b). The baseplate underneath the backstop remains fixed whereas the horizontal mobile baseplate to the front can be moved vertically with maximum offsets of 20 mm (400 m in nature) upwards or downwards. An upward offset of the frontal baseplate constitutes an upward step in the direction of transport, whereas a downward offset produces a downward step (Fig. 6b, c). By using different baseplate configurations, the orientation of the plate contact is varied, specified as angle α that gives the deviation from a frontal step (Fig. 7a). This allows the simulation of abrupt frontal steps (α = 0°) or oblique steps (α = 30˚ and 45˚), analogous to steps in the basement that pre-date JFTB tectonics (Fig. 6).

The mobile backstop can be moved horizontally towards the front of the apparatus, with a maximum displacement (D_{max}) of 35 cm (Fig. 7a, b), corresponding to a shortening of 7800 m in nature. Models featuring frontal steps (except model U10 with a 10 mm upward step, Table 3) are terminated at D = 35 cm. Note that we define the left and right hand side of the model apparatus with regard to the displacement direction of the backstop (Fig. 7a). The backstop is installed 1.3 cm above the fixed baseplate, so that only the sand is compressed without actively squeezing the PDMS/corundum-sand mixture (Fig. 7b).

The sidewalls, front wall, backstop and baseplates are covered with a PVC foil (formerly “Alkor” foil 120010, now available as “Gekkofix 282 11325”, Klinkmüller et al., 2016) that reduces boundary friction. The angle of dynamic stable friction between sand and foil is about 16.5° ± 0.3° (Schreurs et al., 2006). Computer-steered motors ensure precise motion of the backstop and mobile plates. The velocity of the backstop and the mobile baseplate is 10 cm/h for all experiments.

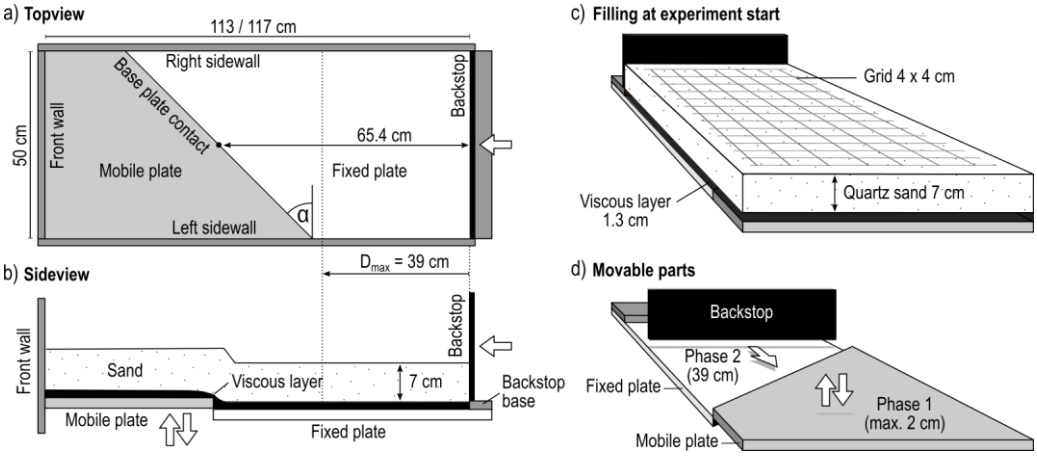

Fig. 7 Schematic representations of the model apparatus. a) Bird's-eye perspective illustrating the 45° oblique baseplate setting. b) Cross-section through the centre of the box, with viscous layer and quartz sand filling. The frontal mobile plate is illustrated with a 20 mm uplift. c) Perspective view without front and sidewalls, illustrating the filling at the start of an experiment and d) perspective view showing movable parts of the apparatus. α: angle of obliquity of the plate contact, with 0° perpendicular to the regional direction of transport (frontal step).

With this experimental set-up, we focus on testing discrete oblique and frontal steps. It is beyond the scope of this study to model the evolution of the whole Jura arc above a fractured basement, or to test local variations of the cover and basal décollement (e.g. thickness or rheological changes). The granular material simulating the Mesozoic cover of the JFTB does not allow for modelling overturned forelimbs of anticlines, since the sand collapses at slopes higher than ~35°. Our models do not include redistribution of granular material by erosion and sedimentation, which can affect the tectonic evolution of structures (e.g. Bonnet et al., 2008; Caër et al., 2018).

5.4 Modelling procedure

Every experimental run starts with a flat baseplate setting. The PDMS/corundum-sand mixture is filled in and a minimum of two days of resting time ensures an even distribution of the viscous layer. The sand layers are sieved in afterwards. A 4 x 4 cm grid of dark corundum sand (Table 1) is added to the final sand surface, which allows tracking surface displacements and rotations (Fig. 7c).

Models that contain a step are conducted in two phases: first, the mobile plate is moved upwards or downwards (max. 20 mm, Fig. 7d). In the second phase (or first and only phase for models without a step), the backstop pushes the sand across the produced step (Fig. 7d). There was no resting time between the two phases. A total of 19 models were completed (Table 3). The models are classified into a downward-step (D), flat-base (F) and an upward-step (U) series (Table 3).

Table 3 List of experiments. A negative throw implies downward steps and a positive throw upward steps. The value α gives the obliquity of the strike of the step with respect to a frontal step (α = 0°). The thickness of the viscous and brittle layers are given in columns five and six respectively. Note that model names indicate the type of a step, specifying throw (for step models) and step obliquity angle α (for oblique steps). A complete overview of all models is shown in Fig. A.1 and Fig. A.2. Abbreviations in model names are D: downward step, F: flat base, U: upward step, CT: computed tomography, RC: reduced cover.

	Model name	Throw [mm]	α	Viscous [mm]	Brittle [mm]
1	D05	-5	0°	14	70
2	D10	-10	0°	13	70
3	D10-30°	-10	30	13	70
4	D20	-20	0°	12	70
5	F1	0	-	14	70
6	F2	0	-	15	70
7	U05	5	0°	14	70
8	U05-30°	5	30	13	70
9	U05-45°	5	45	13	70
10	U10	10	0°	13	70
11	U10-30°	10	30	13	70
12	U10-45°	10	45	13	70
13	U15-30°	15	30	15	70
14	U15-45°	15	45	13	70
15	U20	20	0°	13	70
16	U20-30°	20	30	14	70
17	U20-45°	20	45	13	70
18	U20-45°-CT	20	45	13	70
19	U20-45°-RC	20	45	13	40

5.5 Model analysis

Bird's-eye perspective photographs of the model surface evolution are taken at 1-minute intervals, which translates to a displacement of 1⅔ mm between each image (about 33 m in nature). Videos of all models, except model U20-45°-CT, are provided in the supplementary materials (Schori et al., 2020). After every model run, the sand is removed and the surface of the viscous layer is photographed. Experiment U20-45°-CT is scanned at intervals of 15 minutes using a 64-slice Siemens Somatom Definition AS X-Ray CT scanner, located at the Institute of Forensic Medicine, University of Bern. The scanned cylindrical volume of 104.4 cm length with a diameter of 50 cm is digitised into 3480 circular slices, each with a diameter of 512 pixels. Slices are scanned at a tube setting of 211 mA and 140 kV and exported with an I30 and I70 filter that highlight different parts of the model. We use the software RadiAnt DICOM Viewer V.4.6.8 by Medixant to analyse scans and export cross-sections for illustrations. Note that the viscous layer is poorly distinguishable from the quartz sand in CT-scans and for intermediate model stages (D < 39 cm) of Model U20-45°-CT, the viscous layer is reconstructed based on structural observations after removal of the sand.

6 Analogue model results

6.1 Flat-base models

The flat-base models F1 and F2 serve as a reference for the other models that include a baseplate-step. The first structure in the flat-base models is an imbricate stack that forms in front of the backstop (referred to as backstop imbricate BI, see Fig. 8a-c). The subsequent thrust sheets T1 and T2 forming in front of the BI show leading pop-up structures (Fig. 8c). The BI and thrust sheet T1 are closely spaced and in an evolved stage of T1, its backthrust interferes with the previous structure (Fig. 8c). In each flat-base model, thrust sheets T1 and T2 are identical in their internal architecture and dimension.

In order to compare the structural wedge-development of models, wedge-propagation plots are used (Fig. 8d), which show the evolution of the wedge length L (corresponding to the distance between the backstop and the wedge front) with respect to the backstop displacement D (see Fig. 8c for an illustration of parameters). This representation of data was proposed in Strayer et al. (2001) and called G-grams in Mary et al. (2013). Flat-base models F1 and F2 had slightly different viscous layer thicknesses, which are 14 mm and 15 mm respectively (~280 m and ~300 m in nature). The comparison between flat-base models F1 and F2 (Fig. 8d) shows that the thicker viscous layer leads to longer thrust sheets T1 and T2 (Fig. 8c, d), which in the whole reduces the surface angle of the wedge. This is analogous to critical wedge mechanics (Dahlen, 1990; Davis et al., 1983), where a lower basal friction (i.e. thicker viscous layer) leads to a smaller taper angle of the wedge. Note that thrust fronts of our flat-base models are generally convex to the foreland due to boundary friction at the sidewalls (Fig. 8a), which is characteristic of sandbox-analogue models using a mobile backstop (e.g. Schreurs et al., 2006).

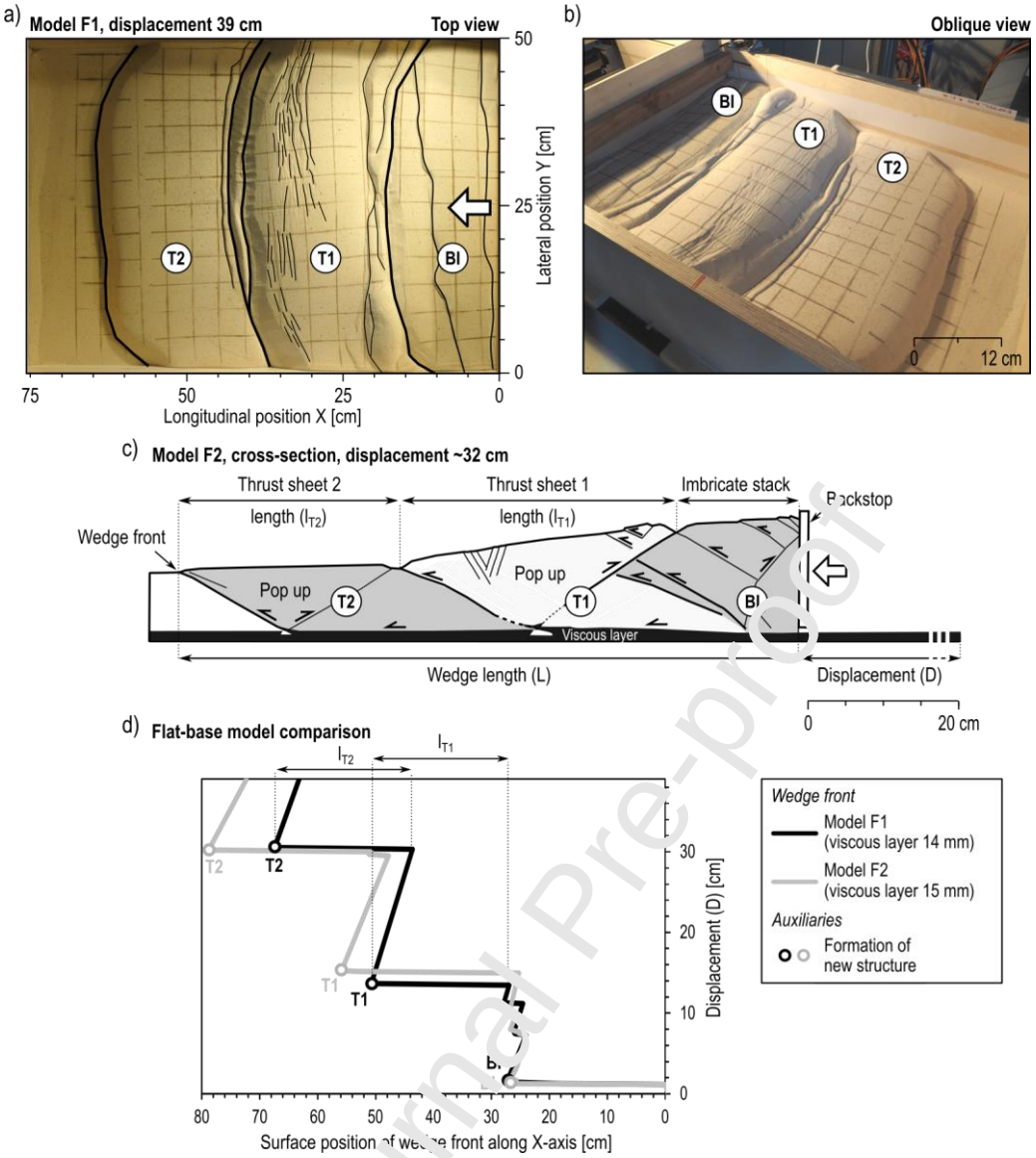

Fig. 8 Analysis of flat-base models. a) Top-view illustrating structures of model F1, which form in sequence from right to left. Two thrust sheets T1 and T2 follow the backstop imbricate stack (BI). The white arrow indicates the direction of compression. b) Oblique view photo of model F1. c) Interpreted cross-section sketch across flat-base model F2 at ~32 cm displacement, illustrating principal structures and parameters. Structural units BI, T1 and T2 are accentuated in different shades of grey. T1 is in an evolved stage, backthrusting the imbricate stack BI whereas T2 just emerges. Note that the wedge front and the length of structures are measured at the model surface. d) Wedge-propagation plot illustrating the difference between flat-base models F1 and F2, of which the latter has a thicker viscous layer that reduces the basal friction. A sudden increase of L is caused by the formation of new structures (BI, T1 and T2). Note that lengths of thrust sheets (l_{T1} and l_{T2}) between models differ. BI adds thrust-slices by frontal accretion, which leads to a jagged graph between X = 24 and 28 cm. BI: Backstop imbricate-stack, T1, T2: Thrust sheet 1 and 2, l_{T1}, l_{T2}: length of thrust sheets T1 and T2 at the surface.

6.2 Evolution of structures related to basement step formation

During vertical movement of the mobile base plate in phase 1, a major reverse fault rooting at the upper step-edge commonly forms in the brittle sand cover. Sub-parallel to that, a minor reverse fault with less offset is seen on CT imagery of model U20-45°-CT, rooting at the lower step edge (Fig. 9a). At a step offset of roughly 10 mm (200 m in nature), the major reverse fault appears on the sand surface. Reverse faults are verging towards the lower baseplate and show inclinations between ca.

55° and 65°. At an offset of ca. 15 mm (300 m in nature), extensional collapse of the quartz sand occurs above the higher plate (Fig. 9a). Fig. 9a shows structures after 20 mm (400 m in nature) upward displacement of the mobile plate. In the case of a 20 mm downward displacement, structures are the same but mirror-inverted. Note that similar reverse faults and collapse structures induced by basement faults are known from seismic lines (Fig. 5).

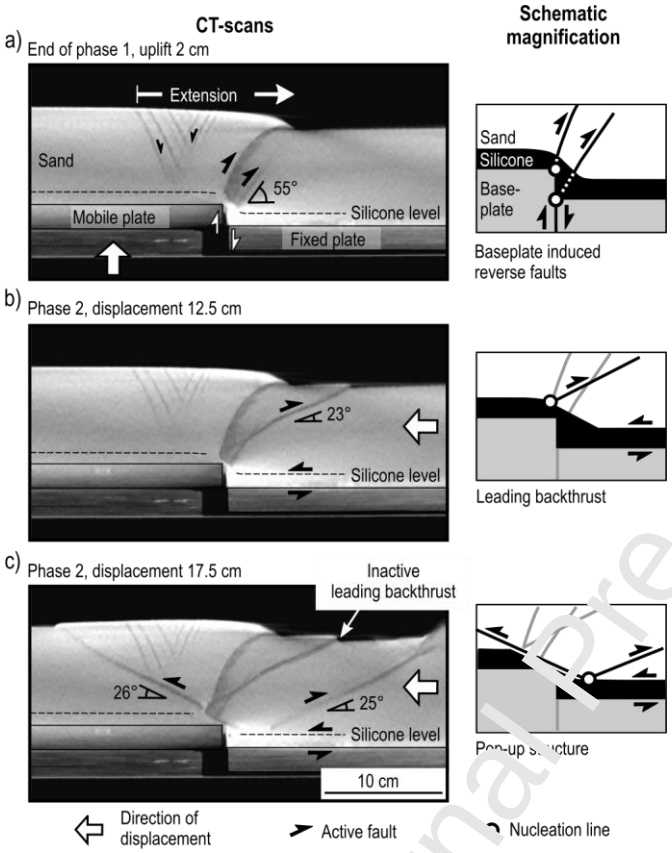

Fig. 9 Cross-sections of CT scans showing step induced structures of model U20-45°-CT, which are representative for the structures in the other models involving steps. a) After 20 mm vertical displacement of the mobile baseplate, an extensional collapse structure is visible in the sand layer. A reverse fault nucleates at the upper step edge and becomes sub-horizontal towards the surface and additionally a blind reverse fault nucleates at the lower step edge. b) After 12.5 cm displacement (D) of the backstop in phase 2, a backthrust nucleating in the viscous layer above the upper step-edge is observed. c) After 17.5 cm displacement (D), structures that formed in phase 1 are embedded in the pop-up of thrust sheet T1. Note that pre-existing faults of phase 1 are not reactivated.

Reactivation of phase 1 faults is not observed during subsequent thin-skinned deformation in phase 2 (Fig. 9b, c), which suggests a high friction angle of these pre-existing faults (Caër et al., 2015). Instead, new thrusts with shallower and mechanically favourable angles between ca. 20° and 33° are formed (Fig. 9b, c). In the case of upward steps with a vertical offset of at least 10 mm (200 m in nature), a backthrust temporarily leading the deformation front nucleates in the viscous layer above the upper step edge (Fig. 9b). Only afterwards, the pop-up structure at the front of thrust sheet T1 appears (Fig. 9c). Note that both the fore- and backthrust of the pop-up structure nucleate above the lower baseplate but the fore-thrust traverses the upper edge of the baseplate step (Fig. 9c). Although genetically different, extensional and compressional structures of phase 1 and 2 are controlled by the same baseplate step and therefore, their position is ultimately linked. In the upward-step model in Fig.

9, structures of phase 1 (Fig. 9a) are embedded in the central and frontal part of the pop-up structure of T1 during phase 2 (Fig. 9b, c). The distinct extensional collapse structure of phase 1 remains in the frontal half of the evolving pop-up structure (Fig. 9c).

6.3 Frontal steps (α = 0˚)

Fig. 10 shows wedge-propagation plots for frontal-step models (α = 0°). In all plots, we add the graph of flat-base model F1 as a reference, in order to infer the influence of baseplate steps. Furthermore, the calculated surface position of step-controlled fore-thrusts (Fig. 9c) and leading backthrusts (Fig. 9b) are plotted in wedge-propagation plots of Fig. 10 (dotted graphs). If abrupt slope changes of solid black graphs (wedge front) coincide with dotted graphs, the wedge front is likely controlled by the step. Nucleation centres of step-controlled thrusts are assumed according to observations in CT-scans (see fault nucleation lines in Fig. 9b, c).

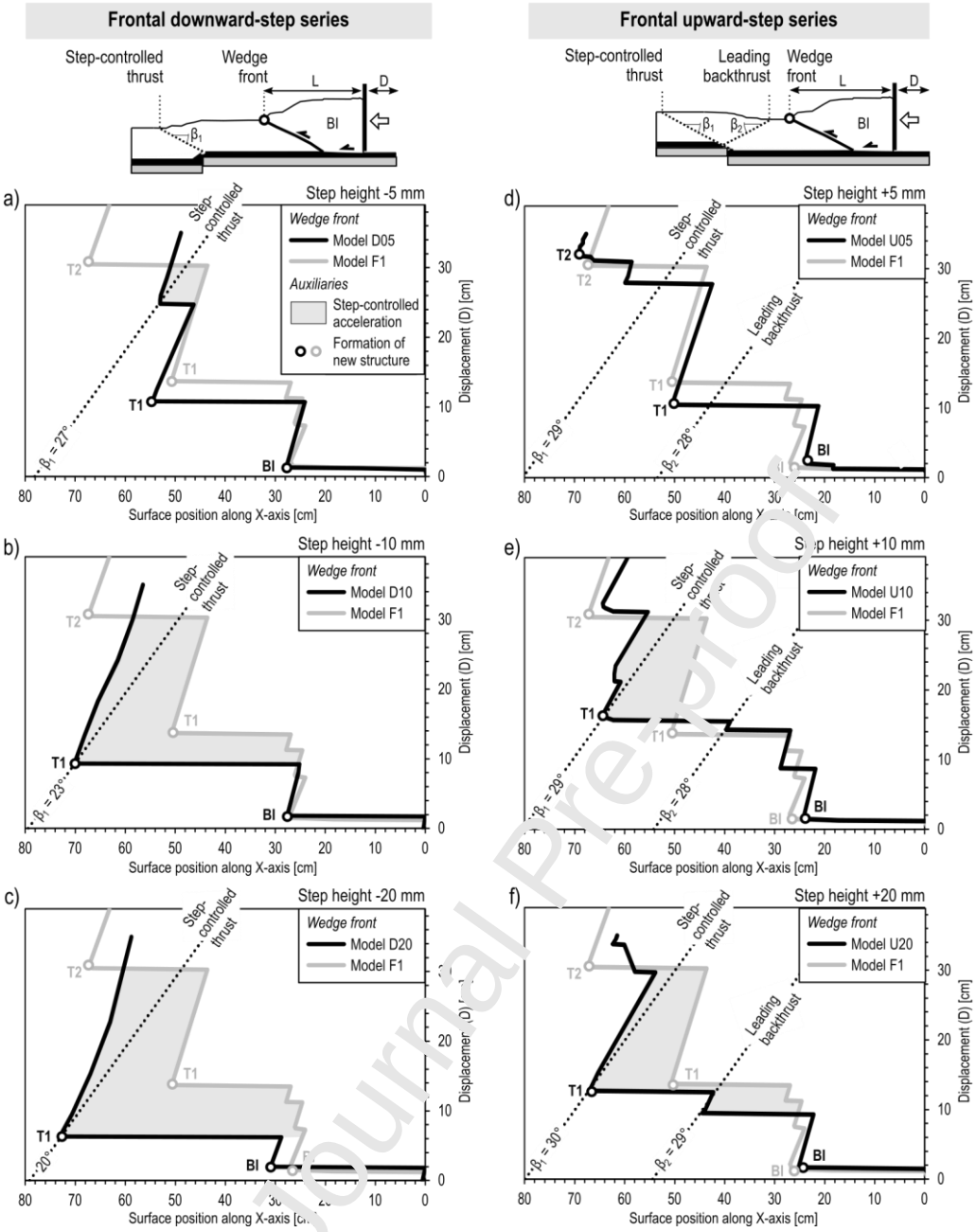

Fig. 10 Wedge-propagation plots of frontal-step models showing compressional phase 2. Cross-sections at the top illustrate parameters after formation of structure BI. The wedge front is the intersection of the foremost active thrust with the sand surface. The surface position along the X-axis indicates the distance to the backstop. Flat-base model F1 (grey graph) is given as reference to evaluate the influence of steps. Dotted graphs plot the calculated surface position of step-controlled thrusts and leading backthrusts for D between 0 and 39 cm. Dip angles of thrusts (β) used to plot the surface positions are indicated at the bottom of dotted graphs. a-c) The downward-step series reveals increasing localisation of the wedge front at higher steps and associated to this, a temporary forward movement of the wedge front. d) The 5 mm high upward step does not control the wedge front. e, f) By contrast, 10 and 20 mm upward steps trigger step-controlled and fore-thrusts and leading backthrusts. D: Displacement of backstop, L: Length of wedge at the surface.

6.3.1 Frontal downward-steps

Frontal downward-step models (Fig. 10a-c) illustrate that with increasing throw of downward steps, thrust sheet T1 forms at less displacement (D) of the backstop and additionally, T1 becomes increasingly larger. In comparison to flat-base model F1, our downward steps therefore lead to a

notable forward advancement of the deformation front (Fig. 10a-c). In an evolved stage however, localisation of deformation at the step prevents downward ramping onto the lower baseplate and inhibits an overall propagation of deformation in comparison to flat-base models (Fig. 10b, c).

After the step-controlled front of T1 has formed in models D10 and D20, backthrusts appear in a backbreaking sequence (see videos in supplementary material, Schori et al., 2020). The overall structure at the front of T1 corresponds to a fault-bend fold with a single thrust-ramp, where backthrusts nucleate (Fig. 11a). The thrust-ramp at the front of T1 roots at the upper edge of the baseplate step and continuous upwards, over the sand of the lower baseplate (Fig. 11a).

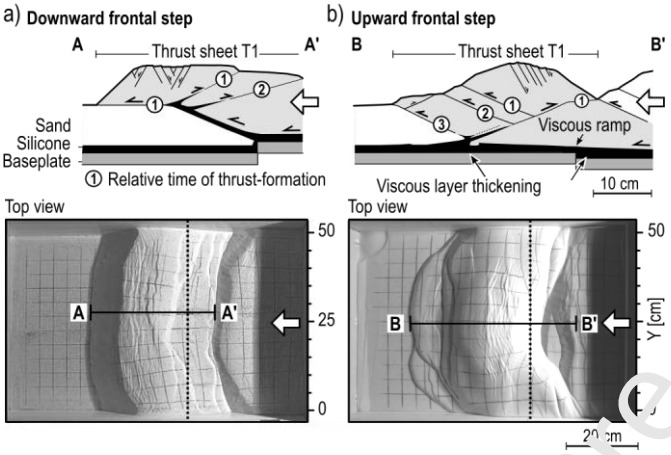

Fig. 11 Step-controlled structures of frontal-step models in phase 2, sketched based on surfaces of the sand and exhumed viscous layer (after removal of sand at the end of the experiment). a) Sketch of model D20, showing a 20 mm downward step. The overall step-controlled structure corresponds to a fault-bend fold that forms backthrusts in a backbreaking sequence, nucleating along the single, main thrust-ramp. b) Sketch of model U10, showing a 10 mm upward step. A pop-up structure nucleates at the step, moves forward and adds frontal thrust-slices subsequently. The step between baseplates is covered by a long viscous ramp with moderate inclination.

6.3.2 Frontal upward-steps

The small upward step of 5 mm (100 m in nature) in model U05 does not trigger thrusts and the overall wedge propagation plot of model U05 is quite similar to flat-base model F1 (Fig. 10d). Upward steps of 10 and 20 mm height (corresponding to 200 and 400 m in nature) localise deformation (step-controlled thrusts), and the deformation front is attracted forwards leading to an enlarged thrust sheet T1 (Fig. 10e, f). In all our upward-step models, a long viscous ramp smoothens the abrupt step between the two baseplates (Fig. 11b) enabling a propagation of deformation onto the higher baseplate (Fig. 11b). Backthrusting becomes increasingly prominent with higher steps (Fig. 10e, f). For one thing, step-controlled leading backthrusts (Fig. 9b) precede the formation of thrust-sheet T1 in models U10 and U20 (Fig. 10e, f). For another thing, the backthrust of the pop-up structure shows concentrated displacement (Fig. 11b) and remains constantly active during shortening of T1. Wedge-propagation plots of models U10 and U20 (Fig. 10e, f) show jagged graphs at the front of thrust sheet T1. This is due to thrust slices that are added at the toe of T1, nucleating beyond the step above the higher frontal baseplate (Fig. 11b). The accretion of thrust-slices distributes deformation among several thrust planes so that individual fore-thrusts absorb notably less displacement than the long-time active

backthrust (Fig. 11a). The overall structure at the front of thrust sheet T1 in model U10 is a pop-up with dominant backthrusting (Fig. 11b) and an imbricated front.

In contrast to downward steps (Fig. 10a-c), thrust sheet T1 in the upward step models forms at about the same displacement (D) of the backstop as observed in flat-base model F1 (Fig. 10d-f) and therefore, forward advancement of the deformation front is due to enlarged thrust sheets only. Note that frontal-step models do not form thrust sheet T2, except for model U05, where the low upward-step of 5 mm does not trigger thrusts (Fig. 10d).

6.4 Oblique downward-step model

Model D10-30° is the only experiment featuring an oblique downward-step (10 mm, at α = 30°, Fig. 12). No downward ramp forms at the transition from the upper to the lower baseplate. Instead, a large fault-bend fold develops that thrusts the sand on the lower baseplate (Fig. 11a). Due to the oblique step, we observe important lateral variations. The deformation front sufficiently close to the oblique step is advanced forward between Y = 0 to 30 cm in Fig. 12a, attracted by the step. As the step controls the deformation front of this segment, the thrust is parallel to the step (Fig. 12a). In flat-base model F1, the position of the regular thrust-front of thrust-sheet T1, which is unaffected by steps, is at X = 10 cm (Fig. 12a). The downward-step model forms a relay thrust that connects the regular thrust position and the forward promoted, step-controlled thrust front. This leads to an initial front of T1, which is a composite of two thrusts that are about 84° oblique to each other (Fig. 12a). We observe an overall angular deformation front that tapers in the direction of transport. Note that in model D10-30˚, no thrust is perpendicular to the direction of displacement (Fig. 12a-c).

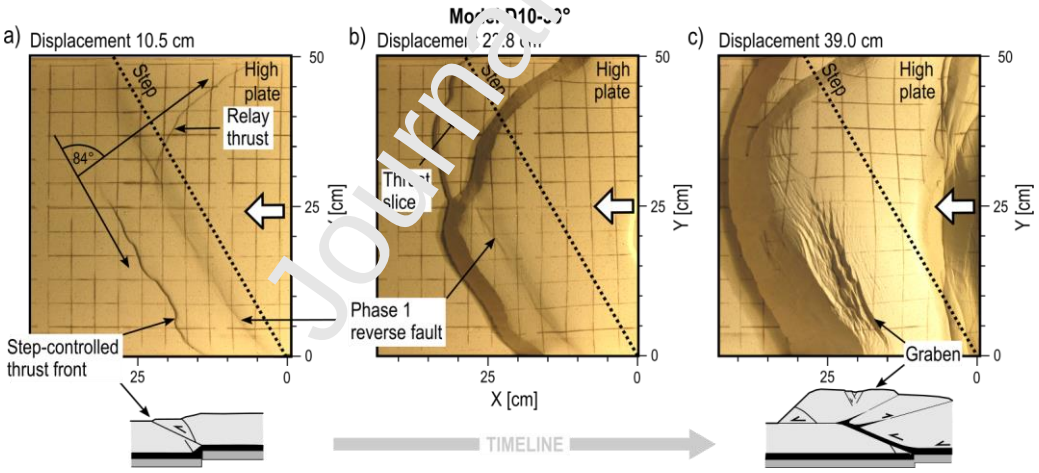

Fig. 12 Top-view photos showing the evolution of structures in model D10-30°, which has a 30° oblique downward-step with a throw of 10 mm. a) The front of thrust sheet T1 nucleates at the step between Y = 0 to 30 cm and therefore, it is parallel to the step. b) A thrust slice is added on the right hand side of the model subsequently. c) Individual oblique thrusts connect to a single thrust front. Due to its large size, the fault-bend fold collapses at the centre forming a graben, parallel to the oblique step.

In our experiment, deformation is step-controlled on the left side (Y = 0 to 30 cm) and afterwards, a thrust slice is added on the right-hand side (Fig. 12b, Y = 25 to 50 cm). The reverse fault remaining from baseplate-offset in phase 1 is passively transported forwards without significant rotation (see lateral position 0 to 25 cm in Fig. 12a, b). In an evolved stage of the experiment, a new graben

structure forms due to extensional collapse roughly in the centre of the large oblique fault-bend fold (Fig. 12c). This graben is sub-parallel to the downward oblique step.

In summary, we observe three step-parallel structures, which are (1) a reverse fault related to vertical baseplate offset in phase 1, (2) an oblique thrust-front of T1 on the left (Fig. 12a, b) controlled by the oblique step during phase 2 and (3) extensional collapse normal faults forming in response to localisation of deformation at the oblique step in phase 2 (Fig. 12c).

6.5 Oblique upward-step models

In the two oblique upward-step series with oblique angles (α) of 30° and 45°, we vary the step throw between 5 and 20 mm (Fig. 13). All oblique upward-step models form oblique viscous-ramps between the lower and higher baseplates (Fig. 11b). Above these continuous ramps, different oblique structures form in the brittle sand cover. These structures reveal step-controlled thrust segments that nucleate near the baseplate step and are therefore parallel or sub-parallel to the step. With increasing step throw, step-controlled thrusts on the sand surface are more numerous (Fig. 13).

6.5.1 30° oblique-step series

At a low oblique upward-step height of 5 mm (100 m in nature), thrust sheet T1 remains a continuous structure with virtually no imbrication (Fig. 13a). The frontal thrust of T1 in Fig. 13a is step-controlled on the left, roughly between Y = 0 to 15 cm. In an evolved model stage, this leads to a continuous, *bow-shaped* front of thrust sheet T1 (Fig. 13a, late stage). Note that flat-base model F1 (Fig. 8a) is notably less bow-shaped than U05-30° (Fig. 13a), illustrating that the bow shape is not a mere cause of boundary effects.

Model U10-30° (Fig. 13b), with a 30° oblique-upward step and a throw of 10 mm (200 m in nature), develops thrust slices that pinch out laterally and reveal curved fronts, resulting in distinct *crescent-shaped* structures (Fig. 13b, late stage). These thrust-slices are added at the toe of the wedge, alternatingly on the left and right hand side. Crescent-shaped thrust-slices nucleate in the viscous layer on the upper plate, commonly beyond the step. With increasing throw of the oblique step, curved thrusts become less numerous in favour of angular thrusts (Fig. 13c, d). Therefore, at step throws of 15 and 20 mm (300 to 400 m in nature), individual thrust-slices are reminiscent of triangles (Fig. 13c,d). The left side of angular thrusts (left limb of triangle) mirrors the orientation of the step and nucleates at the upper step-edge, thus representing a step-controlled feature (Fig. 13c, d).

At the highest oblique upward-step of 20 mm (400 m in nature), step-controlled thrust segments are initially sub-parallel to the step (Fig. 13d, early stage), but rotate clockwise with progressive deformation (Fig. 13d, late stage). The thrust segment between Y = 20 to 25 cm in Fig. 13d (early stage), forms as a relay oblique-thrust that is ca. 80° oblique to the step and also distinctly oblique to the direction of transport (Fig. 13d). The relay thrust connects the step-controlled thrust front above the upper baseplate with the trailing regular thrust-front on the lower baseplate.

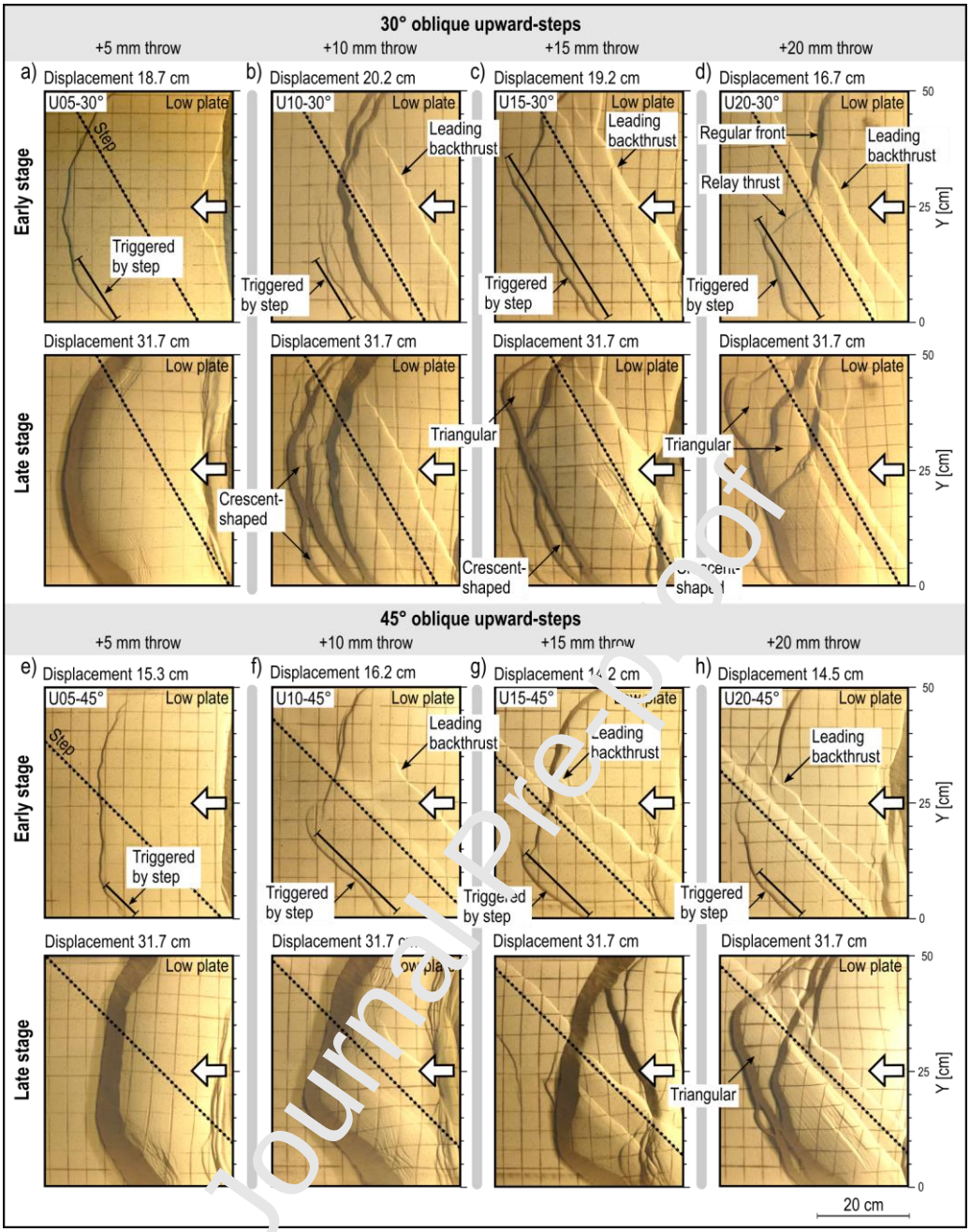

Fig. 13 Evolution of step-controlled structures with increasing throws for 30° (a-d) and 45° oblique upward-steps (e-h). a) A 30° oblique step with a low throw (5 mm) leads to a continuous structure which is step-controlled between Y = 0 to 15 cm. b) With increasing step throw, imbrication increases and thrusts are curved. c) Angular thrusts with step-controlled left sides are accompanied by curved thrusts. d) At a 30° oblique step and a high throw of 20 mm, the thrust front between Y = 0 to 20 cm is step-controlled, whereas on the right between Y = 25 to 50 cm, the regular thrust front lags behind. A relay oblique thrust connects both fronts. e-g) At 45° oblique upward-steps with throws of 5 to 15 mm, the front of T1 is continuous but asymmetric, being step-controlled on the left side. h) At a high 45° oblique step with a throw of 20 mm, imbrication of T1 occurs.

6.5.2 45° oblique-step series

At step throws of 5 to 15 mm (100 to 300 m in nature) in 45° oblique-step models, the thrust front of T1 is continuous, but becomes increasingly asymmetric and angular with higher step throws (Fig. 13e-g). The left sides of these continuous thrusts nucleate above the upper step-edge and are step-controlled

features (Fig. 13e-g, early stage). Only at a high step throw of 20 mm (400 m in nature), the 45° oblique-step model shows imbrication of thrust sheet T1 (Fig. 13h).

6.5.3 Difference between 30° and 45° oblique steps

We observe a fundamental difference between 30° and 45° oblique-step models at intermediate step heights of 10 and 15 mm (200 to 300 m in nature, Fig. 13b, c, f, g). The overall wedge-length evolution plots of 30° oblique-step models show a notable influence of the step (Fig. 14a, b), whereas the wedge-length plots of 45° oblique-step models resemble flat-base model F1 (Fig. 14c, d). For one thing, this difference is because 30° oblique steps cause a strong frontal imbrication of thrust sheet T1 at a step height of 10 and 15 mm (Fig. 13b, c), which is not the case for 45° oblique steps with the same throws (Fig. 13f, g). For another thing, instead of adding thrust-slices to T1, deformation propagates forwards in the 45° models and a new thrust-sheet T2 forms similar to flat-base models (Fig. 14c, d).

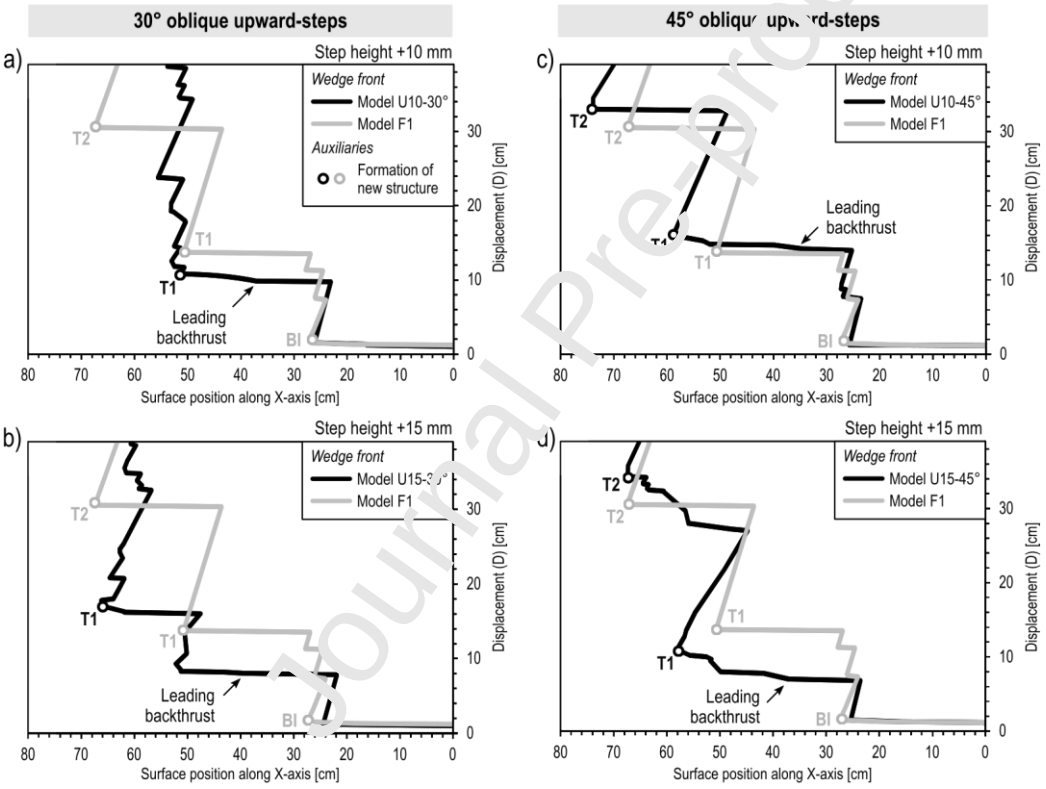

Fig. 14 Wedge-propagation plots for 10 and 15 mm high oblique upward-step models. Note that the wedge-length (L) is given with respect to the front-most thrust measured on the sand surface. a, b) Plots of 30° oblique upward-step models differ considerably from flat-base model F1, featuring strong imbrication of thrust sheet T1 and absence of thrust sheet T2. c, d) Plots of 45° oblique upward-steps resemble flat-base model F1, because both thrust sheets T1 and T2 form and imbrication is virtually absent.

6.5.4 Leading backthrusts

At 30° and 45° oblique upward-steps of 10 to 20 mm (200 to 400 m in nature), we observe step-controlled leading backthrusts (Fig. 13) that temporarily constitute the front of the wedge, preceding T1 (also see Fig. 9b, c). In bird's eye perspective, leading backthrusts are relatively long, stretching the entire width of 30° oblique-step models (e.g. Fig. 13c, d). They are distinctly step-parallel and become

inactive after only 1 to 3 cm displacement and subsequently, they are dissected during imbrication of thrust sheet T1 (Fig. 13c, d, late stage). Since leading backthrusts are step-controlled features that hardly experience subsequent rotation (Fig. 13d, f), they constitute excellent indicators for the orientation of oblique steps, even in an evolved stage of models (Fig. 13).

6.5.5 Lineament rotation

Step-controlled thrusts start forming on the left side of our oblique-step models and append sequentially along the step (Fig. 15a). This is typically accompanied by crescent-shaped thrust slices that are added on the left wedge front (Fig. 15a, b), seemingly to compensate an asymmetric deformation front, and resulting in an overall thrust front that becomes more perpendicular to the direction of transport. When triangular thrust-slices append, their step-controlled left segments connect to a single lineament (Fig. 15a) that shows an overall clockwise rotation about a vertical axis over time. This rotation is strongest for high upward steps in models U20-30° and U20-45°, where we measure a rotation of 12° and 15°, respectively of step-controlled fore-thrusts (see Fig. 15a, b).

Table 4 shows observed rotations at different step throws. In contrast to step-controlled fore-thrusts, step-controlled leading backthrusts do not reveal any noticeable rotations (see Fig. 15a, b, sequence number 2).

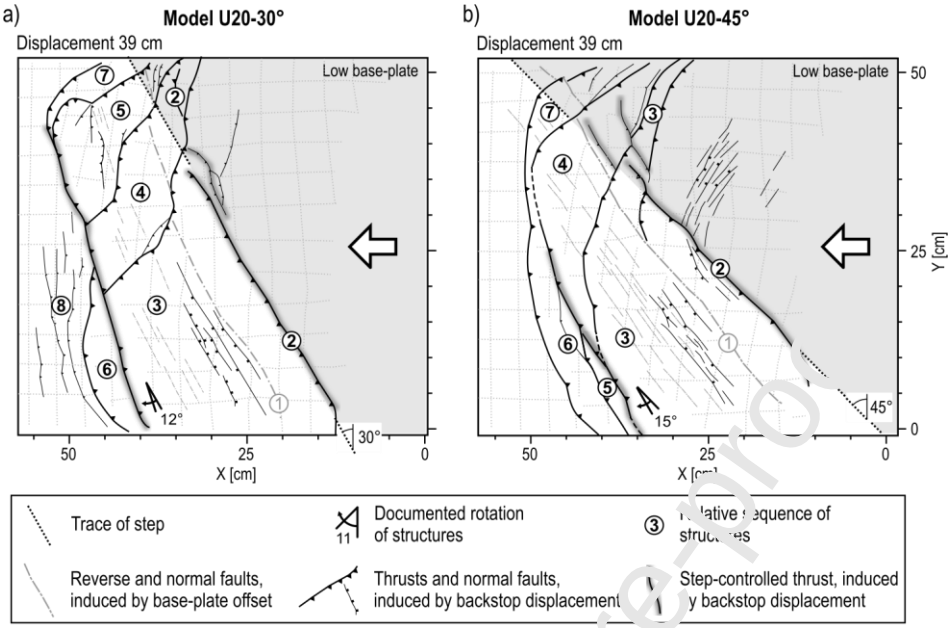

Fig. 15 Line drawings of top-views illustrating the relative sequence of structures in models U20-30° and U20-45°. Structures are (1) reverse faults forming in phase 1, (2) step-controlled leading backthrusts, (3) initial pop-up structures and (4) first triangular thrust-slices. Subsequent structures vary between the two models. a) In the model U20-30° featuring a 30° oblique step, structure (5) is another triangular thrust-slice (6) and (7) follow as crescent-shaped thrust-slices whereas structures (8) are thrusts associated with small buckle folds. b) In comparison to this, at the 45° oblique step of U20-45°, structures (5) to (7) are crescent-shaped thrust-slices.

Table 4 Overview of observed clockwise rotations of step-controlled fore-thrusts over time. A negative throw denotes a downward step whereas positive throws indicate upward steps. α: Obliquity of step.

Step	Rotation of thrust	
Throw	α = 30°	α = 45°
-10 mm	<1°	-
5 mm	*4°	*13°
10 mm	8°	*6°
15 mm	10°	*3°
20 mm	12°	15°

* No imbrication of thrust sheet T1

6.6 CT-scanned oblique upward-step model

Model U20-45°-CT is a CT-scanned rerun of model U20-45°, featuring a 20 mm (400 m in nature) upward-step of 45° obliquity. The CT scans allow the reconstruction of cross-sections at different model stages (Fig. 16). Raw CT-scan sections interpreted for Fig. 16 are compiled in the supplementary material of this article (Schori et al., 2020).

Structures of phase 1 (Fig. 16a) are fragmented laterally and at depth during horizontal shortening, and transported forwards embedded in the front of thrust sheet T1 (compare to Fig. 16c and d). In contrast to this, late collapse structures due to sediment stacking are situated at the back of thrust sheet T1 and not at the front (e.g. Fig. 16d, cross section B4 and C4).

The front of thrust sheet T1 is step-controlled on the left side (Fig. 16b, cross-sections D2 and E2) whereas the right hand side is yet unimpeded by the step (Fig. 16b, cross-section A2). By comparison, pop-up structures in cross-sections D2 and E2 (Fig. 16b) lie slightly more frontwards, attracted by the upward oblique-step, which results in an overall curved thrust front, visible on the top view image in Fig. 16b.

The thrust-slice added in cross-sections B3 to E3 (Fig. 16c) corresponds to a triangular thrust-slice in top-view images of Fig. 16c, d. Cross-sections C3 and D3 (Fig. 16c) illustrate that on the left side, the triangular thrust-slice nucleates near the step, whereas in C4 to D4 (Fig. 16d), the subsequent crescent-shaped thrust-slice nucleates beyond the step. The backthrust of pop-up structure T1 is permanently active whereas fore-thrusts become inactive when new thrust-slices are added to the front of the wedge (e.g. compare cross-sections A2 to A4, Fig. 16).

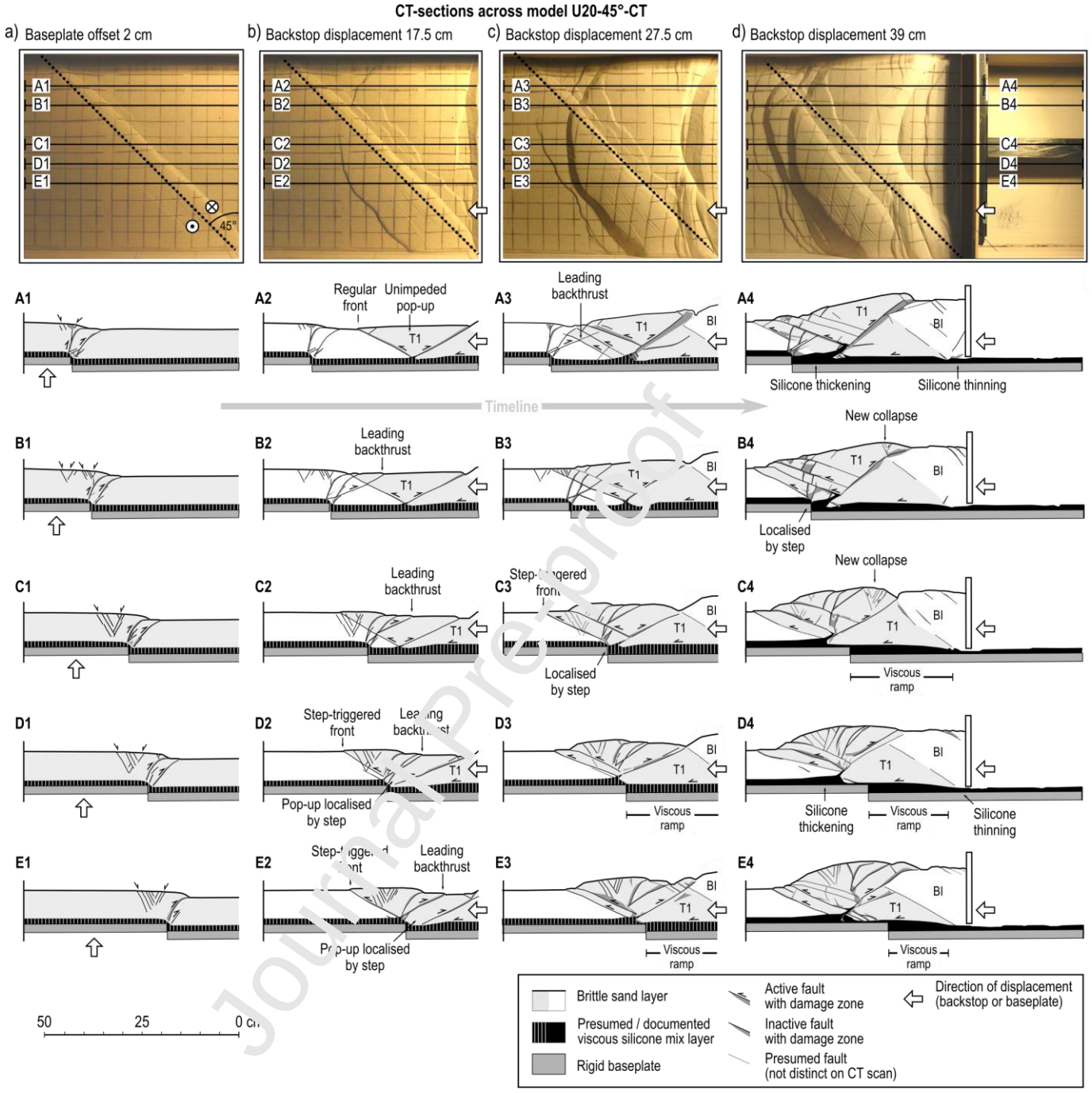

Fig. 16 Interpreted CT-sections across model U20-45°-CT, showing five sections at different model stages. a) The first stage shows the model after baseplate-offset phase 1. An extensional collapse structure and two reverse faults form in the sand cover in response to vertical offset of the baseplates. b) The front of thrust sheet T1 reveals a pop-up, which is localised by the step in cross-sections D2 and E2. c) Thrust-slices are added to the front of T1. d) The final stage gives detailed insight into structures of the viscous layer. A viscous ramp is documented in cross-sections C4, D4 and E4. The along-strike length of the ramp varies laterally. BI: Backstop imbricate stack, T1: Thrust sheet 1.

6.6.1 Formation of viscous ramps

In all models, viscous material thins out underneath the backstop imbricate fan BI (Fig. 16d), which is the structure showing most sand stacking and therefore, the vertical load exerted on the PDMS/corundum-mixture by the overburden is highest. Consequently, viscous material flows forward with no material escaping backwards through the gap between the backstop and the baseplate (Fig.

16d). In upward-step models, the forward flowing viscous material accumulates in two locations. First, thickening occurs underneath the front of the pop-up structure of T1 (Fig. 16d, section A4). Secondly, upward steps cause an accumulation of viscous material on the lower baseplate, between the step and the roots of BI, thereby forming a long viscous ramp with moderate inclination (Fig. 16d, C4 to E4). Since the length of the ramp depends on the spacing between the step and BI, the length of the viscous ramp varies laterally (Fig. 16d, C4 to E4) and furthermore, over time with ongoing displacement of the backstop (Fig. 16a to d). Note that if the step-throw exceeds the thickness of the viscous layer (e.g. step height 15 or 20 mm, 300 or 400 m in nature), the formation of the viscous ramp ultimately leads to in-situ uplift of a few millimetres. Above the edge of the upper baseplate, the viscous layer thins out down to a few millimetres (Fig. 16d, C4 to E4).

6.7 Oblique upward-step model with reduced cover

Model U20-45°-RC tests a 20 mm (400 m in nature) oblique upward-step with a reduced sand cover of 40 mm instead of 70 mm (Fig. 17a, b). The thinner sand cover leads to shorter and more numerous thrust sheets and generally smaller thrust-slices in comparison to a cover thickness of 70 mm (Fig. 17c), which is directly related to the geometric relationship between layer thickness and thrust-fault dip-angle (Allemand and Brun, 1991). However, similar step-controlled features as observed in models with a high oblique upward-step and a sand thickness of 70 mm are present, such as triangular thrust-slices and a step-controlled leading backthrust (Fig. 17a). In the model, an overall sigmoidal structure is the result of triangular thrust-slices of variable size that grow sequentially (Fig. 17a, b). The overall step-controlled front of connected triangular thrust-slices rotates by about 15° clockwise (Fig. 17b).

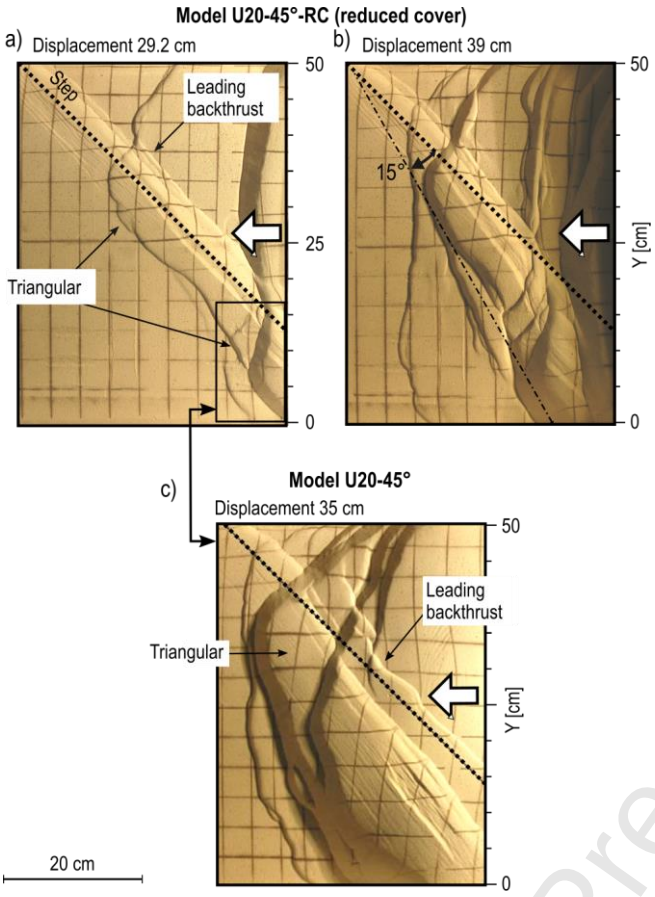

Fig. 17 Top view photographs of model U20-45°-RC, featuring a 45° oblique ramp, 20 mm step-throw and a reduced sand thickness of 40 mm. a) The left side of the large triangular thrust slice is initially parallel to the step. b) In the final stage, an overall sigmoidal shape results from connected triangular thrust-slices. c) Top view of model U20-45°, featuring a 70 mm thick sand cover and therefore showing larger but similar structures as model U20-45°-RC.

7 Discussion

7.1 Summary of model results

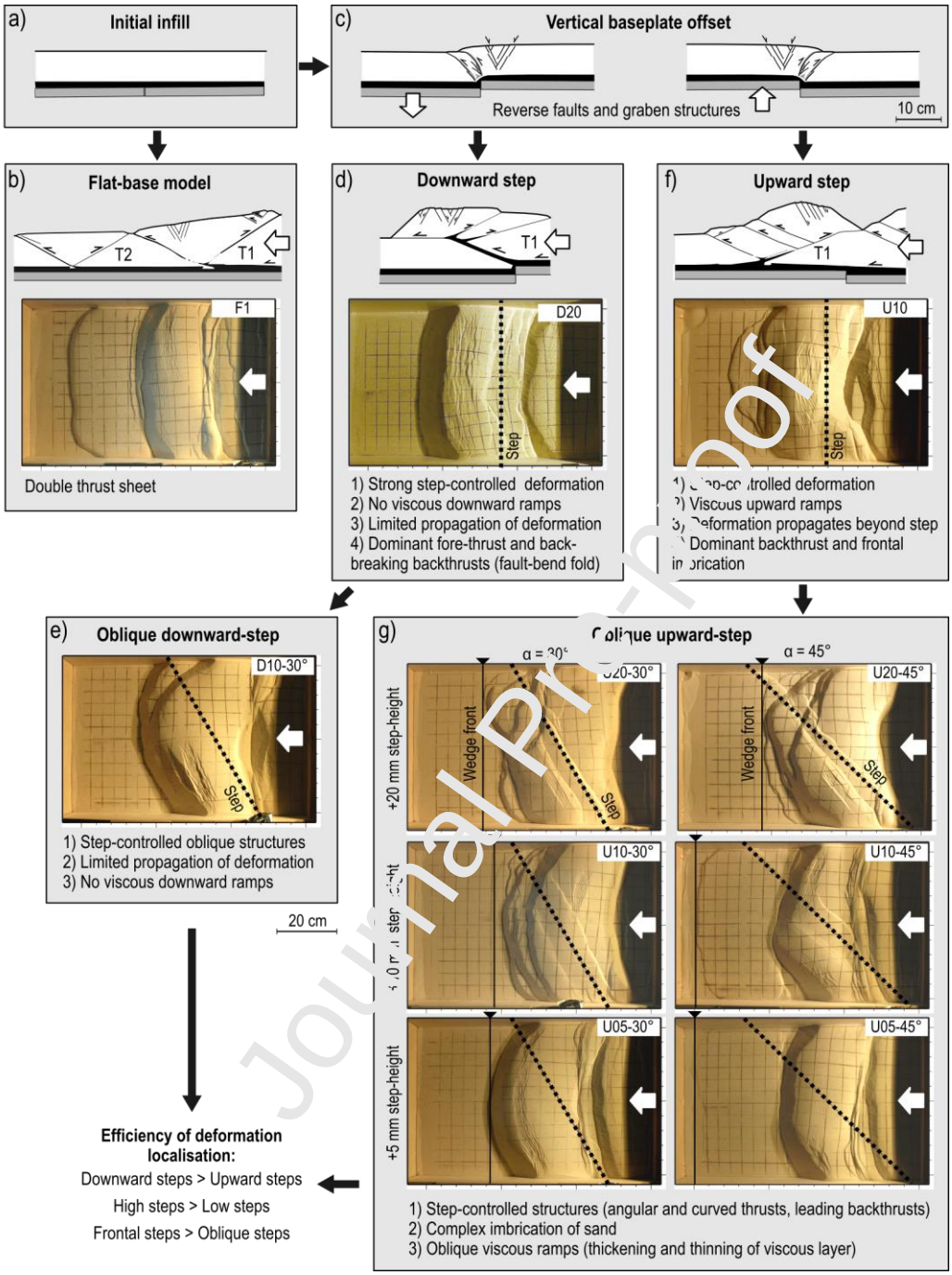

Fig. 18 Summary of experiments and first-order step-controlled structures. An overview of the final surface structures of the different model set-ups is presented in the Appendix (Fig. A.1 and Fig. A.2), and the original data are compiled in the supplementary material (Schori et al., 2020).

An overview of experiments and the first order influence of upward and downward steps is summarised in (Fig. 18). Flat-base models (Fig. 18a, b) develop two similar thrust sheets (T1 and T2) with notable less stacking of granular material than observed in step models and there is no imbrication of thrust sheets. Vertical offset of baseplates (Fig. 18c) induces graben structures and

reverse faults in the brittle sand cover. During subsequent thin-skinned compression, both downward and upward steps attract and localise deformation, which stimulates a fast forward propagation of deformation in an early stage, but retains the overall deformation in a late stage. Downward steps (Fig. 18d) show exceedingly strong localisation of deformation preventing the formation of viscous downward ramps and overall propagation of deformation onto the lower baseplate. Instead, fault-bend folds with thrusts nucleating above the upper edge of the downward step form at the front of thrust sheet T1 (Fig. 18d). An oblique downward-step (Fig. 18e) controls the formation of fault-bend folds with oblique frontal thrusts. Numerical and analogue downward-step models of Caër et al. (2018) show that with sufficient shortening at step-controlled thrusts under the right mechanical conditions (high friction angle of cover sediments and low friction angle of décollement layers), deformation can propagate onto the lower baseplate.

The localisation of deformation at upward steps is less efficient than for downward steps. In comparison to downward steps, upward steps (Fig. 18f) feature smooth viscous ramps that enable a propagation of deformation onto the higher baseplate. Thickening of viscous material is therefore indicative for upward steps. The brittle cover shows dominant backthrusts and frontal imbrication (Fig. 18f). Oblique upward-step models (Fig. 18g) reveal a more complex imbrication of brittle structures, featuring asymmetric thrust slices and step-controlled thrust segments that rotate up to 15° about a vertical axis. In contrast to this, oblique viscous ramps remain continuous structures.

Higher oblique steps increase deformation localisation and step-controlled thrust segments become more important, overall leading to angular structures (Fig. 18g, U20-30° and U20-45°). 45° oblique steps cause less localisation of deformation (less imbrication and faster wedge-propagation) than 30° oblique steps. Consequently, the efficiency of deformation-localisation does not depend on step height alone, but also on the angle of obliquity (α) of the upward-step.

In summary, the effect of deformation localisation at steps is (i) stronger at high steps than at low steps, (ii) stronger at downward steps than at upward steps and (iii) stronger at frontal steps than at oblique steps.

7.2 Comparison to previous oblique-ramp models

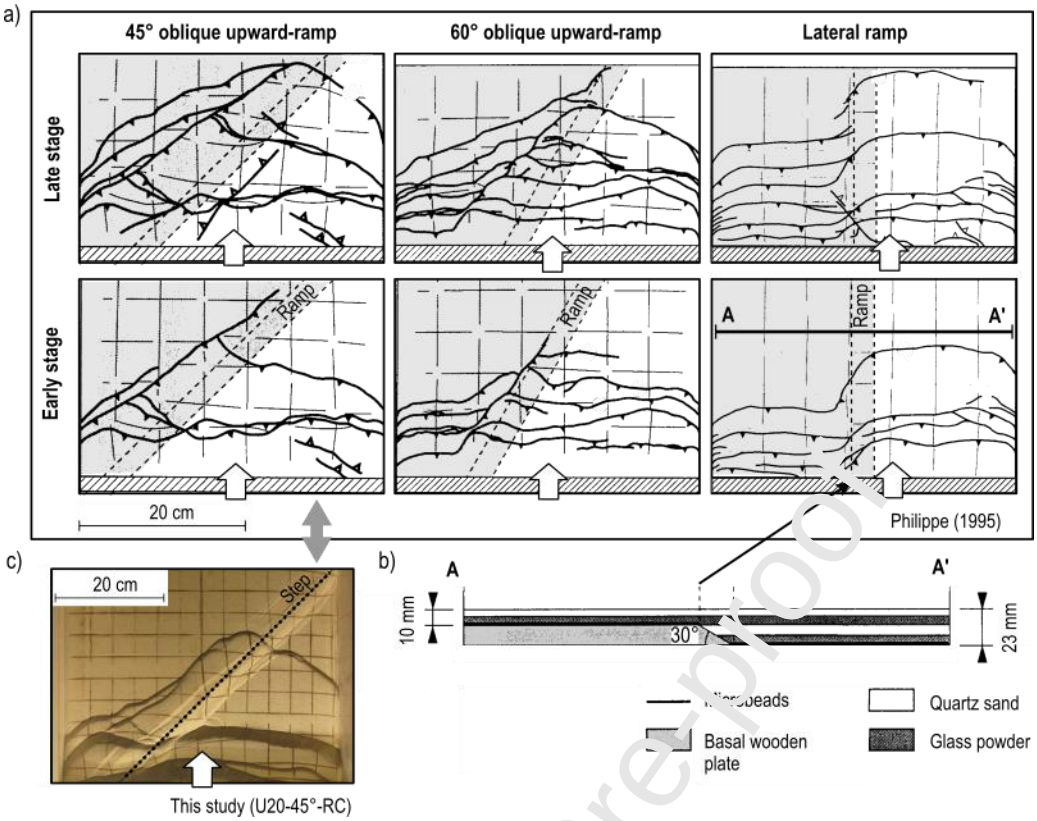

Fig. 19 a) Oblique and lateral-ramp analogue sandbox-models of Philippe (1995). b) Cross-section through the lateral ramp model illustrating a basal wooden plate that enforces a rigid ramp of 30°. A thin layer of microbeads provides the basal décollement. c) Model U20-45°-RC featuring a thin brittle layer shows remarkably similar structures as the 45° oblique upward-step model of Philippe (1995) in an early stage.

Previous models on oblique ramps in the Jura Mountains were carried out by Philippe (1995, see Fig. 19a). In contrast to our models, the baseplate geometry in Philippe (1995) provides an enforced, rigid ramp with an inclination of 30° (Fig. 19b). The brittle cover is thinner above the higher basal wooden plate (Fig. 19b) and no precursory baseplate-offset phase is simulated. Furthermore, the basal décollement is modelled using a thin layer of microbeads (Fig. 19b) and therefore, no viscous flow occurs. However, the top-view pattern of the early stages of the 45° oblique-ramp model of Philippe (1995) is very similar to the pattern forming in the 45° oblique-step model with reduced brittle cover U20-45°-RC of this paper (Fig. 19c). In addition to 45°-oblique rigid ramps, Philippe (1995) tested 60° oblique ramps as well as lateral ramps (Fig. 19a), showing that with increasing obliquity, triangular thrust-slices disappear in favour of thrust-sheets with a rather straight front perpendicular to the transport direction.

Our experiments demonstrate that deformation localisation at oblique steps is the reason for triangular structures. Therefore, the absence of such triangles in 60° oblique-step models (Fig. 19a) suggests reduced deformation localisation with increasing step-obliquity (α). Extrapolated, this suggests that lateral steps show the least localisation of deformation and frontal upward-steps the most.

7.3 Local and regional rotations of structures

Step-controlled fore-thrusts in our models reveal local rotations about a vertical axis of up to 15° over time (e.g. Fig. 17, Fig. 15), related to localisation of deformation at individual baseplate steps. The sketch in Fig. 20 shows a schematic overview of rotations of step-controlled thrusts deduced from observations in our models, with a transport direction and basement-step orientations matching typical cases in the JFTB. Note that step-controlled oblique structures are local anomalies within a regional trend of structures. The Central and Eastern Jura show a regional clockwise rotation of 7° to 8° (Laubscher, 1965, 1961), whereas regional counter-clockwise rotation is proposed for the Southern Jura (Affolter, 2004; Philippe, 1994). These regional rotations are more broadly linked to lateral displacement gradients across the Jura arc (Affolter, 2004). Regional and local rotations in the JFTB have a different origin; they were competing and have to be distinguished.

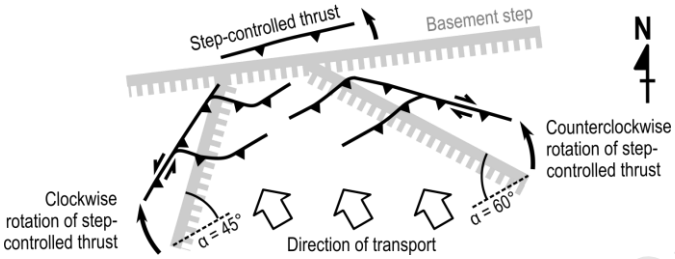

Fig. 20 Rotation scheme for thin-skinned thrusts that are controlled by pre-existing oblique upward-steps, derived from observations of our analogue models and those by Philippe (1995). The sketch fits typical directions that may occur in the JFTB, with basement faults striking NNE-SSW, ENE-WSW and NW-SE, and a transport direction to the NW.

7.4 Natural examples of step-controlled structures

Our analogue models show that sufficiently high oblique steps ultimately lead to step-controlled oblique structures, such as sigmoidal, curved or angular thrusts viewed from above (e.g. Fig. 17b, Fig. 18g). In the tectonic map of Fig. 21a, we point out exemplary zones in the JFTB, where we propose oblique structures, associated with pre-existing basement faults that acted as structural controls. These zones are described with sketches (Fig. 21b) outlining the proposed tectonic linkage between basement faults and corresponding thin-skinned structures in the cover. Note that sketches in Fig. 21b illustrate thin-skinned structures of the JFTB, which formed during Mio-Pliocene times above a basal décollement in Triassic evaporites. Therefore, oblique structures were also transported several kilometres north-westwards after their formation, at least in the Internal Jura (see displacements indicated in Fig. 21a).

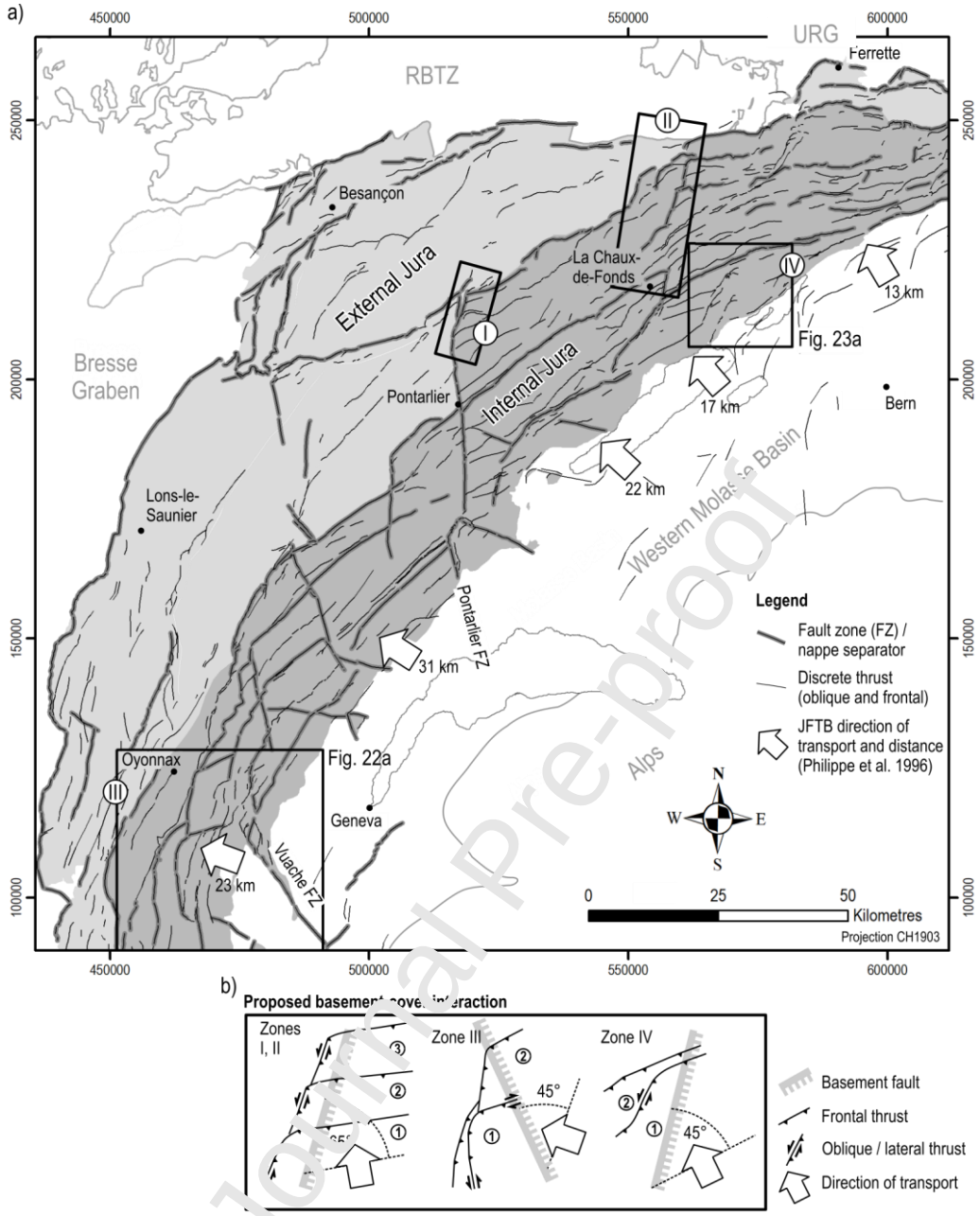

Fig. 21 a) Overview of faults in the Mesozoic cover across the JFTB. Zones in the Internal Jura with notable occurrences of oblique-thrust systems are marked with black rectangles. The tectonic map contains an updated structural interpretation, using available geological vector maps of France (BRGM, 2004) and Switzerland (Swisstopo, 2012) as well as high-resolution digital elevation models (IGN-F, 2018; Swisstopo, 2011). b) Structural interpretations illustrating pre-existing basement steps (thick, grey normal faults) that trigger thrusts in the Mesozoic cover (black thrusts). Numbers indicate the relative sequence of structures. RBTZ: Rhine-Bresse Transfer Zone, URG: Upper Rhine Graben.

7.4.1 Zones I and II – Pontarlier fault zone and Internal Jura north of La Chaux-de-Fonds

Zone I in Fig. 21a marks the northern termination of the Pontarlier fault zone. Angular thrusts are observed and folds parallel to NNE-SSW trending sinistral strike-slip faults reveal the thrusting component of oblique ramps. We interpret this system as a connection of oblique and lateral ramps that constituted the western lateral limits of thrust-sheets of the Internal Jura (Fig. 21b, zone I). It follows that the Pontarlier sinistral fault zone was contemporaneously active to folding and thrusting,

and does not represent a late structural feature of the Jura Mountains. This agrees with previous suggestions by Laubscher (1961).

Zone II to the north of the town of La Chaux-de-Fonds (Fig. 21a) shows angular and overlapping thrusts. Therefore, similar to zone I, we propose NNE-SSW striking oblique basement-steps that triggered the observed structures in the Mesozoic cover (Fig. 21b). The sketch for zones I and II in Fig. 21b correlates with structures of analogue models of Philippe (1995) featuring 60° oblique upward-steps, where laterally confined triangular thrust-slices are absent (Fig. 19a).

7.4.2 Zone III - Oyonnax-Vuache

Zone III (Fig. 21a) lies in the Southern Jura Mountains and an enlargement is depicted in Fig. 22a. The Vuache fault zone in the southern part of Fig. 22a reveals oblique ramps that are indicative of step-controlled structures and a NW-SE trending basement step. A connection to pre-JFTB tectonic features has also been proposed in previous studies (Laubscher, 1981; Philippe et al., 1996).

A distinct triple-nappe system south of Oyonnax comprises two triangular nappes and a more crescent-shaped nappe (Fig. 22a), which bears resemblance to our analogue model U20-45°, featuring a 20 mm (400 m in nature) 45° oblique upward-step (Fig. 22b). In analogy to model U20-45°, we propose a NW-SE trending basement fault for the structures that formed in zone III (Fig. 21b). Within the 45° oblique-step series, triangular thrust-slices occur at the highest throw of 20 mm only (Fig. 13h) and accordingly, we infer a basement step for the natural example of at least 400 m. This is in agreement with a seismic line interpretation across Oyonnax-Champfromier (Guellec et al., 1990), which reveals a basement high with a throw of several hundreds of metres, SE of Oyonnax (Fig. 22c). Whether this basement high formed by post-Jura inversion or rather represents a horst that predates the Jura Mountains (see tectonic solutions addressed in Guellec et al., 1990), remains debated. However, as thrust geometries in Fig. 22a are strongly suggestive of an oblique-step in the basement, our study supports the latter solution. In addition, a direct comparison between the natural example and our analogue model (Fig. 22a, b) suggests a probable structural evolution as depicted in Fig. 22a. Note that a pre-JFTB normal fault in the basement does not rule out a subsequent inversion of the basement in recent times.

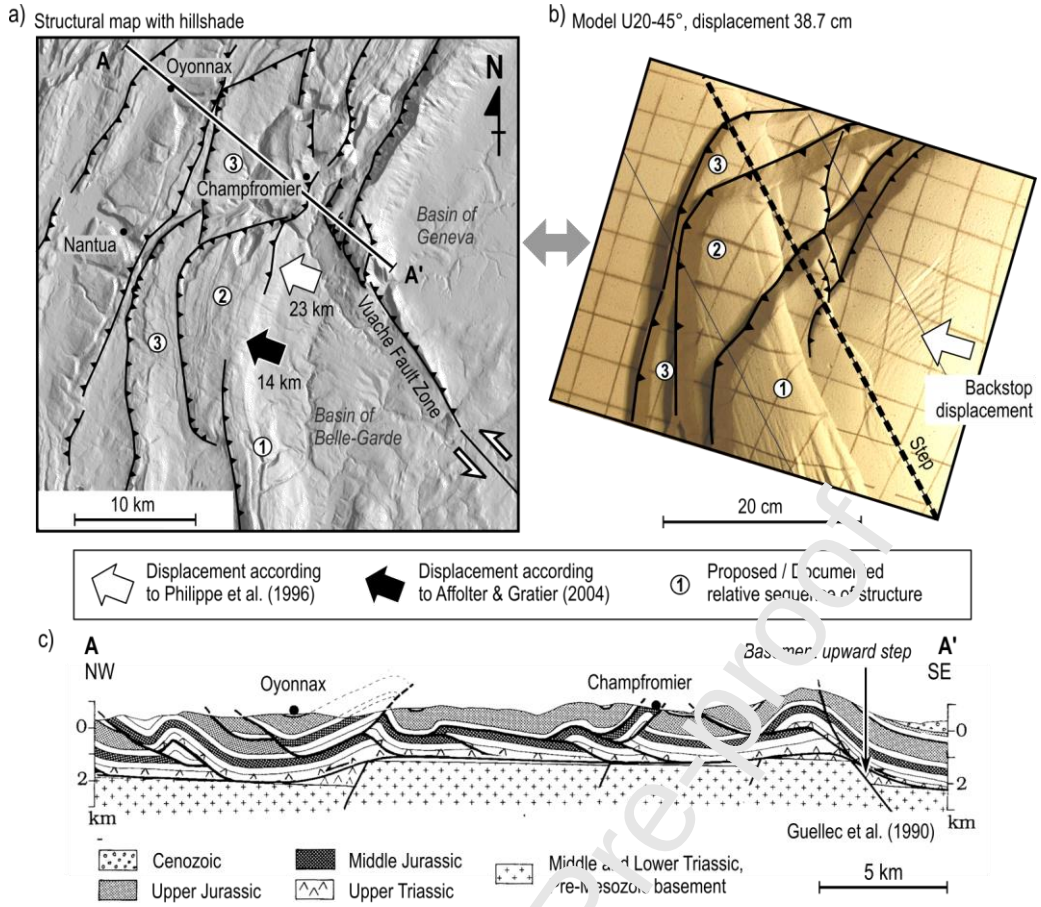

Fig. 22 Natural example in the Internal Jura, Zone III - Oyonnax-Vuache (location in Fig. 21a). a) Hillshade model derived from NASA (2014) in the area of Oyonnax with highlighted main thrusts. b) Model U20-45° shows similar triangular structures as the natural example in the area of Oyonnax. c) Cross section from Guellec et al. (1990) based on a seismic survey, showing a basement high underneath Champfromier.

7.4.3 Zone IV - Chasseral Anticline

Zone IV (Fig. 21a) lies in the Internal Jura and comprises the Chasseral anticline, which contains an oblique fold-segment in respect to JFTB transport directions (see magnification in Fig. 23a). The overall structure in Fig. 23a is remarkably similar to our 45˚ oblique upward-step model with a reduced cover U20-45°-RC (Fig. 23b). The comparison between the model (Fig. 23b) and the natural example (Fig. 23a) suggests that the curved shape of the Chasseral anticline is connected to a NNE-SSW trending basement fault. This supports previous suggestions by Lüthi (1954), Laubscher (2008b) and Meier (2010). We furthermore deduce a high basement step of about 400 m for the natural example, as the best-fit model U20-45°-RC features a 20 mm upward step. Based on our model (Fig. 23b), we also deduce a rough relative sequence of structures for the natural example (Fig. 23a). Note that the basement structure that controlled the oblique Chasseral anticline lies between 9.5 to 16 km to the southeast, according to different displacement models of Affolter and Gratier (2004) and Philippe et al. (1996), respectively.

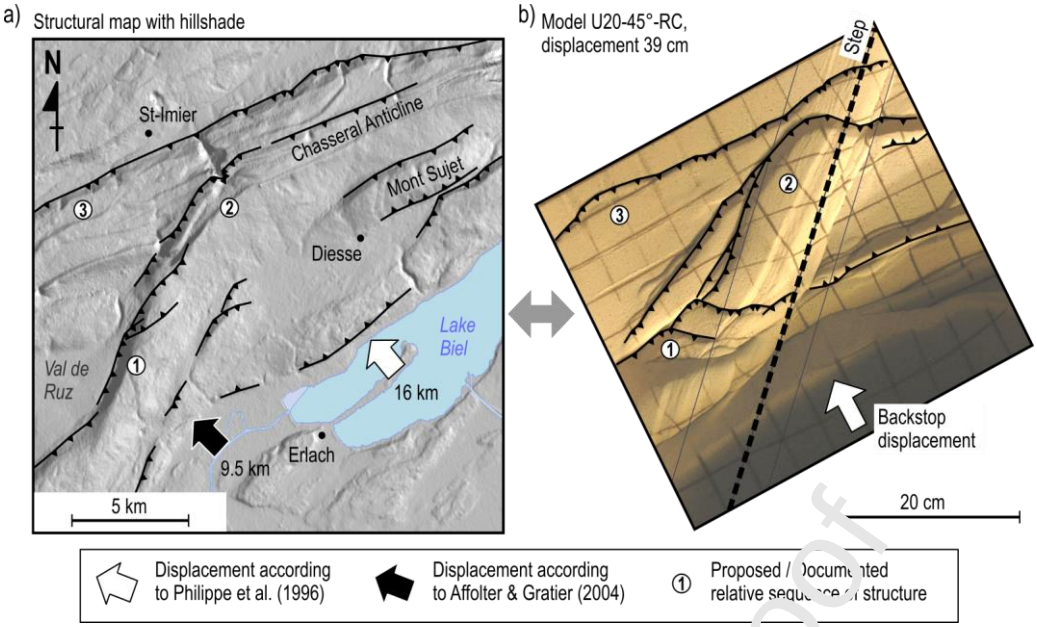

Fig. 23 Natural example in the Internal Jura, Zone IV - Chasseral anticline (location in Fig. 21a). a) Hillshade model derived from NASA (2014) in the area of St-Imier and Lake Biel with highlighted main thrusts. b) Model U20-45°-RC shows similar structures as the natural example.

7.5 Summary of natural structures

We propose the presence of pre-JFTB normal faults in the basement with NW-SE (Hercynian) and NNE-SSW (Rhenish) orientations that provided trigger lines for thin-skinned structures in the Internal Jura (Fig. 22, Fig. 23). The orientations of these basement faults suggest Palaeozoic Variscan fault systems, which were reactivated during Mesozoic and Cenozoic times. This led to important basement offsets that controlled the thin-skinned deformation in Miocene and Pliocene times. The tectonic events that come into question for fault reactivations are the opening of the Alpine Tethys rift system in Jurassic times (Stampfli et al., 1998; Ziegler, 1988b), Eo-Oligocene graben formation in connection with the ECRIS (Illies, 1972; Michon, 2000) and Eocene to Miocene evolution of the Alpine flexural foreland basin (Burkhard and Sommaruga, 1998; Laubscher, 1992).

Our models suggest that basement offsets in the examples in the Internal Jura (Fig. 22, Fig. 23) must reach at least 400 m in order to control the formation of triangular nappes or thrust-slices during Mio-Pliocene thin-skinned formation of the JFTB. Smaller basement throws rather led to continuous but curved or angular anticlines with few imbrication (e.g. Fig. 13a, e, f, g), such as for example the Graitery anticline in the Eastern Jura (Fig. 3b). Step-controlled structures were displaced up to about 30 km north-westwards during JFTB formation (Affolter, 2004; Philippe et al., 1996). Therefore, graben structures and reverse faults in the Mesozoic cover, which formed due to pre-JFTB basement extension, are allochthonous and do not overlie their original basement fault.

Basement structures were undoubtedly present before the formation of the JFTB and controlled thin-skinned structures. In addition, seismic surveys and earthquakes show that the area of the Jura Mountains and surrounding was under the influence of thick-skinned compression after the main thin-skinned JFTB stage until today, which caused local basement inversion (Caër, 2016; Edel et al., 2006;

Lacombe and Bellahsen, 2016; Madritsch et al., 2008; Ustaszewski and Schmid, 2007). Recent inversion may be related to tectonic underplating in connection with an equilibration of the Alpine wedge (Mosar, 1999) and/or lithospheric long-wavelength buckling (Bourgeois et al., 2007; Lefort and Agarwal, 1996).

8 Conclusions

Thin-skinned deformation of the JFTB during Mio-Pliocene was locally pre-conditioned by steps (faults) in the pre-Mesozoic basement (Laubscher, 1961). By means of brittle-viscous analogue sandbox-models, we study the formation of step-controlled structures. Our models involve the formation of steps between rigid baseplates, overlain by a viscous layer at the base of a brittle sand layer. The brittle sand layer is subsequently pushed horizontally across the step. We subsequently compare our model results to natural examples. The following important observations characterise the deformation style:

- Initial vertical baseplate offset induces reverse faults and extensional collapse structures in the brittle cover that nucleate at the step and above the higher plate. A reactivation of these initial structures is not observed during subsequent horizontal compression.
- During subsequent horizontal compression, pre-existing steps in the rigid footwall trigger step-controlled thrusts, because they localise deformation in a different position due to stress perturbations. Localisation of deformation results in a fast forward propagation of deformation in an early stage but inhibits propagation later.
- Downward steps lead to the formation of fault bend folds with considerable duplication of the brittle cover. In contrast, upward steps control pop-up structures with imbricated fronts, dominant backthrusts and long viscous ramps with moderate inclinations.
- The effect of deformation localisation at baseplate steps is stronger at high steps than at low steps, stronger at downward steps than at upward steps and stronger at frontal steps than at oblique steps.
- 30° and 45° oblique upward steps lead to imbrication with laterally confined thrust-slices. Imbrication and angular thrusts, pointing into the direction of transport, are more abundant with increasing step-height. Angular thrusts are composed of two oblique-thrust segments, with one side that is step-controlled and the other side forming a relay thrust that connects to the regular trailing thrust front. Laterally confined, triangular thrust-slices are characteristic for 30° and 45° oblique steps (this study), but they are absent at oblique steps of 60° and more (Philippe, 1995).
- Upward oblique-step models with high step throws of 20 mm (400 m in nature) reveal vertical rotations of up to 15° of step-controlled fore-thrusts. Step-controlled leading backthrusts hardly rotate and provide excellent indicators for the orientation of oblique steps.
- Frontward flow of viscous material during thin-skinned deformation has important consequences for upward-step dynamics. In particular, viscous ramps form in front of upward-steps, assisting deformation to propagate onto the upper plate. Subsequently, the viscous ramp ensures the transition of more material onto the upper baseplate without forming new step-controlled structures in the cover. Viscous ramps are dynamic structures, adapting their length laterally (in

the case of oblique upward-steps) and over time. Accumulation of viscous material occurs in front of upward steps and towards the front of the wedge. Oblique viscous ramps are large continuous structures whereas the overlying brittle layer may show strong imbrication.

We find good correlations of model structures with oblique structures in the Internal Jura (Fig. 22 and Fig. 23). Correlations allow inferring the rough orientation and throw of pre-existing basement steps in nature that controlled thin-skinned deformation. In particular, our models support a NNE-SSW striking oblique upward-step with a throw of 400 m that controls the Chasseral anticline and a NW-SE striking oblique upward-step with a throw of 400 m controlling the Oyonnax-Vuache nappe system. Step-controlled structures of the Internal Jura are transported several kilometres north-westwards, away from the basement step that induced deformation. Therefore, step-controlled structures need a palinspastic restoration to identify the position of a corresponding basement step. Model-to-nature comparison of step-controlled oblique structures can also be a powerful tool to assess the relative age of basement structures. An important basement high was for example documented on a seismic line across the Internal Jura (Guellec et al., 1990), but interpretations did not unambiguously reveal whether the basement high formed before or after the JFTB. Correlations with our models strongly support that the basement high predates the JFTB and controlled characteristic oblique structures in the cover. Examples from the JFTB highlight the importance of analysing structures of fold-and-thrust belts in all three dimensions, and our model results may be of use for interpreting fold-and-thrust belts from around the globe.

Acknowledgements

This study was financed by the University of Fribourg as part of the PhD research project of the first author. We express our gratitude to Nicole Schwenderer of the Institute of Forensic Medicine (University of Bern) for assisting us with the CT scanner. Furthermore, we are indebted to Anna Sommaruga for sharing her expertise on the Jura Mountains. Sandra Borderie is thanked for critically scrutinising our modelling parameters and for discussions on the effect of pre-existing basement faults. We would also like to thank the reviewers, Pauline Souloumiac and Alexander Malz, as well as the editor Philippe Agard for their helpful and constructive comments.

Funding: This work was supported by the University of Fribourg, Department of Geosciences, Earth Sciences, Switzerland; and the University of Bern, Institute of Geological Sciences, Switzerland.

Appendix

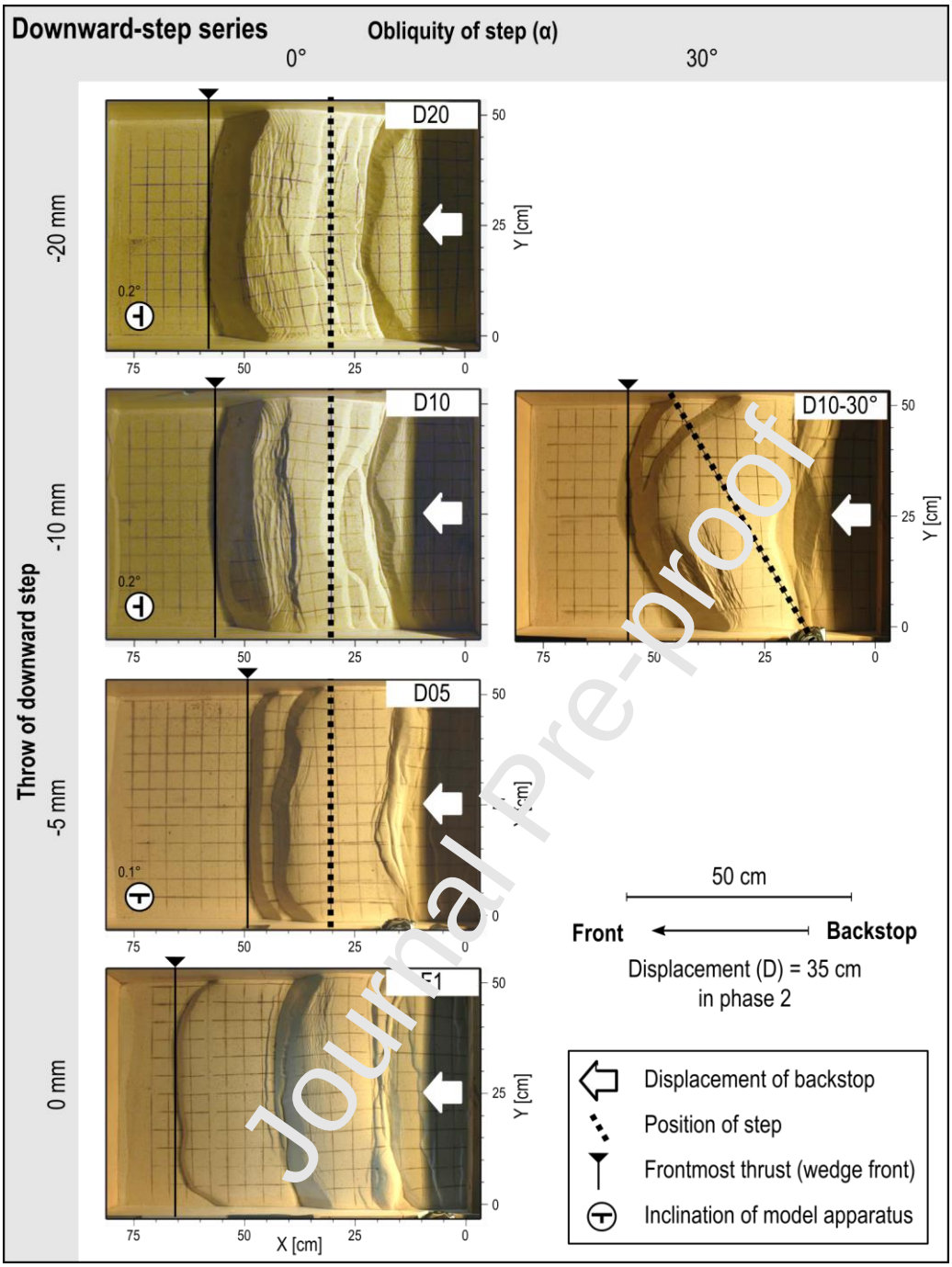

Fig. A.1 Overview of downward-step models showing top-view photos at a consistent displacement D = 35 cm. Slight inclinations of the model apparatus have no detectable influence. Even the small downward step of 5 mm already controls deformation exceedingly and outweighs uneven distributions of viscous material.

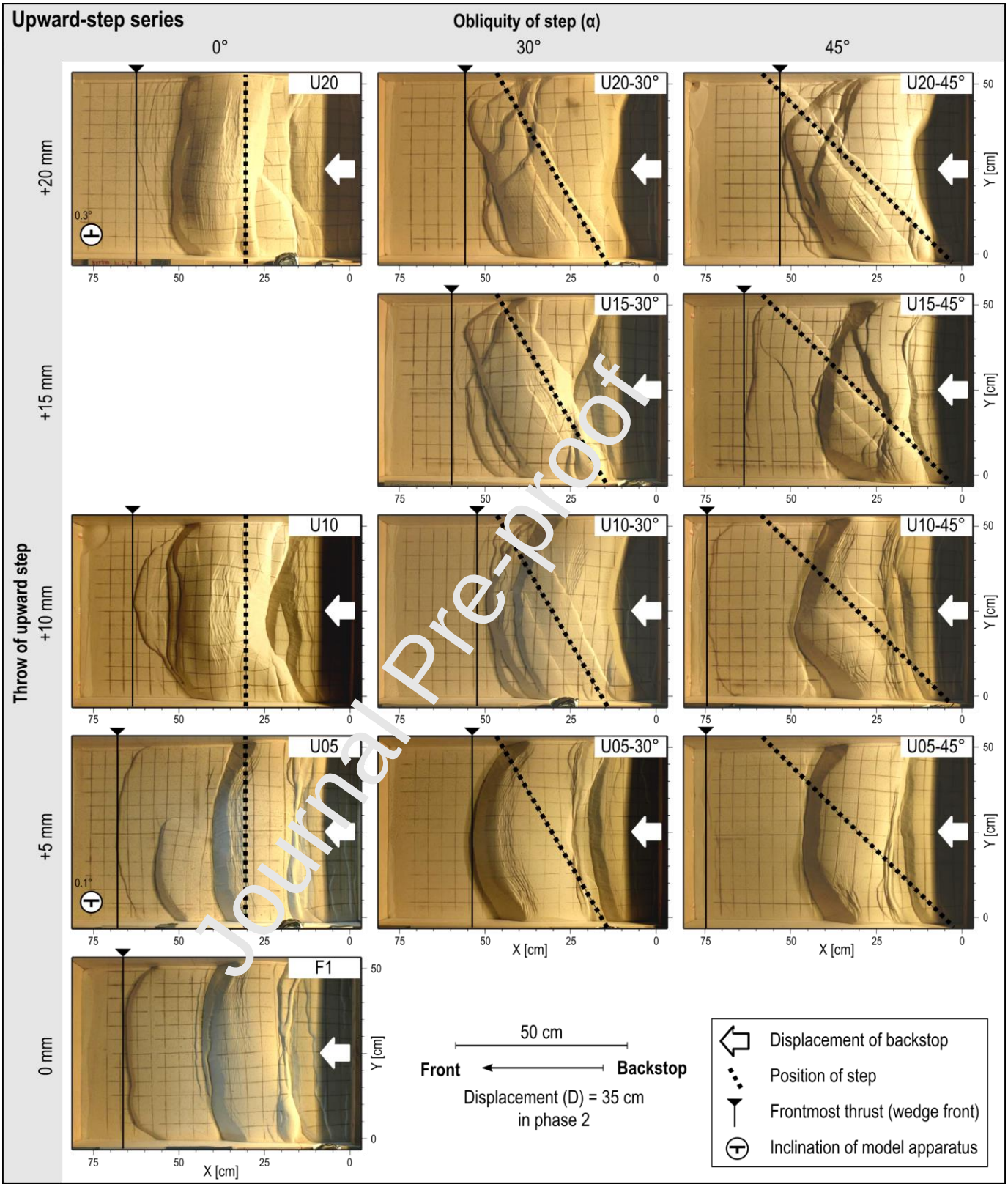

Fig. A.2 Overview of upward-step models showing top-view photos at a consistent displacement D = 35 cm. In experiments U05 and U20, the model apparatus is slightly tilted along the long axis. This causes an asymmetric distribution of viscous material, which is slightly thicker (less friction) on the plunging side. Models U05 and U20 consequently develop asymmetric structures.

References

Affolter, T., 2004. Map view retrodeformation of an arcuate fold-and-thrust belt: The Jura case. J.

Geophys. Res. 109, B03404. https://doi.org/10.1029/2002JB002270

Allemand, P., Brun, J.P., 1991. Width of continental rifts and rheological layering of the lithosphere. Tectonophysics 188, 63–69. https://doi.org/10.1016/0040-1951(91)90314-I

Allenbach, R.P., Wetzel, A., 2006. Spatial patterns of Mesozoic facies relationships and the age of the Rhenish Lineament: A compilation. Int. J. Earth Sci. 95, 803–813. https://doi.org/10.1007/s00531-006-0071-0

Apotria, T.G., Snedden, W.T., Spang, J.H., Wiltschko, D. V., 1992. Kinematic models of deformation at an oblique ramp, in: Thrust Tectonics. Springer, pp. 141–154. https://doi.org/10.1007/978-94-011-3066-0_12

Aubert, D., 1971. Le Risoux, un charriage jurassien de grandes dimensions. Eclogae Geol. Helv. 64, 152–156. https://doi.org/10.5169/seals-163975

Becker, A., 2000. The Jura Mountains - an active foreland fold-and-thrust belt? Tectonophysics 321, 381–406. https://doi.org/10.1016/S0040-1951(00)00089-3

Bellahsen, N., Mouthereau, F., Boutoux, A., Bellanger, M., Lacombe, O., Jolivet, L., Rolland, Y., 2014. Collision kinematics in the Western external Alps. Tectonics 33, 1055–1088. https://doi.org/10.1002/2013TC003453

Berberian, M., 1995. Master 'blind' thrust faults hidden under the Zagros folds: active basement tectonics and surface morphotectonics. Tectonophysics 241, 193–224. https://doi.org/10.1016/0040-1951(94)00185-C

Bergerat, F., Cazes, M., Damotte, B., Guellec, S., Mugnier, J.-L., Roure, F., Truffert, C., 1989. Les structures distensives en Bresse d'après les données du profil sismique Jura-Bresse (programme ECORS). Comptes rendus l'Académie des Sci. Série 2, Mécanique, Phys. Chim. Sci. l'univers, Sci. la Terre 309, 325–332.

Bergerat, F., Mugnier, J.-L., Guellec, S., Truffert, C., Cazes, M., Damotte, B., Roure, F., 1990. Extensional tectonics and subsidence of the Bresse basin: an interpretation from ECORS data, in: Roure, F., Heitzmann, P., Polino, R. (Eds.), Deep Structures of the Alps. Mém. Soc. géol. suisse, pp. 145–156.

Bièvre, G., Mercier, E., 2010. The 'Bois du Peu' thrust sheets (external French Jura mountains): re-examining the concept of 'Fault-Fold'. HAL-INSU Arch. Ouvert. insu-00442.

Boigk, H., Schöneich, H., 1974. Perm, Trias und älterer Jura im Bereich der südlichen Mittelmeer-Mjösen-Zone und des Rheingrabens, in: Illies, J.H., Fuchs, K. (Eds.), Approaches to Taphrogenesis: Proceedings of an Nternational Rift Symposium Held in Karlsruhe, April 13-15, 1972 - Inter-Union Commission on Geodynamics, Scientific Report. Schweizerbart, Stuttgart, Germany, pp. 60–71.

Bonnet, C., Malavieille, J., Mosar, J., 2008. Surface processes versus kinematics of thrust belts:

impact on rates of erosion, sedimentation, and exhumation - Insights from analogue models. Bull. la Société Géologique Fr. 179, 297–314. https://doi.org/10.2113/gssgfbull.179.3.297

Bourgeois, O., Ford, M., Diraison, M., Le Carlier de Veslud, C., Gerbault, M., Pik, R., Ruby, N., Bonnet, S., 2007. Separation of rifting and lithospheric folding signatures in the NW-Alpine foreland. Int. J. Earth Sci. 96, 1003–1031. https://doi.org/10.1007/s00531-007-0202-2

BRGM, 2004. Cartes géologiques à 1/50000 format 'vecteurs'. Bureau de recherches géologiques et minières (BRGM).

Burkhard, M., 1990. Aspects of the large-scale Miocene deformation in the most external part of the Swiss Alps (Subalpine Molasse to Jura fold belt). Eclogae Geol. Helv. 83, 559–583. https://doi.org/10.5169/seals-166602

Burkhard, M., Sommaruga, A., 1998. Evolution of the western Swiss Molasse basin: structural relations with the Alps and the Jura belt, in: Mascle, A., Puigdefabregas, A., Luterbacher, H.P., Fernandez, M. (Eds.), Geological Society Special Publication. Geological Society Special Publications, pp. 279–298. https://doi.org/10.1144/GSL.SP.1998.134.01.13

Buxtorf, A., 1916. Prognosen und Befunde beim Hauenstein-basis- und Grenchenbergtunnel und die Bedeutung der Letzteren für die Geologie des Juragebirges. Verhandlungen der Naturforschenden Gesellschaft Basel 27, 184–254.

Buxtorf, A., 1907. Zur Tektonik des Kettenjura. Bericht der Versammlung des Oberrheinischen Geol. Vereins 40, 29–38.

Caër, T., 2016. Interprétation structurale et équilibre mécanique: Le calcul à la rupture appliqué aux chaînes d'avant-pays. Dr. thesis. Université de Cergy-Pontoise.

Caër, T., Maillot, B., Souloumiac, P., Leturmy, P., de Lamotte, D.F., Nussbaum, C., 2015. Mechanical validation of balanced cross-sections: The case of the Mont Terri anticline at the Jura front (NW Switzerland). J. Struct. Geol. 75, 32–48. https://doi.org/10.1016/j.jsg.2015.03.009

Caër, T., Souloumiac, P., Maillot, B., Leturmy, P., Nussbaum, C., 2018. Propagation of a fold-and-thrust belt over a basement graben. J. Struct. Geol. 115, 121–131. https://doi.org/10.1016/j.jsg.2018.07.007

Chauve, P., Perriaux, J., 1974. Le jura, in: Debelmas, J. (Ed.), Géologie de La France: Les Chaînes Plissées Du Cycle Alpin et Leur Avant-Pays. Doin, Paris, pp. 443–464.

Coward, M.P., De Donatis, M., Mazzoli, S., Paltrinieri, W., Wezel, F.C., 1999. Frontal part of the northern Apennines fold and thrust belt in the Romagna-Marche area (Italy): Shallow and deep structural styles. Tectonics 18, 559–574. https://doi.org/10.1029/1999TC900003

Dahlen, F.A., 1990. Critical taper model of fold-and-thrust belts and accretionary wedges. Annu. Rev. Earth Planet. Sci. 18, 55–99. https://doi.org/10.1146/annurev.ea.18.050190.000415

Davis, D., Suppe, J., Dahlen, F.A., 1983. Mechanics of fold-and-thrust belts and accretionary wedges. J. Geophys. Res. Solid Earth 88, 1153–1172. https://doi.org/10.1029/JB088iB02p01153

Debrand-Passard, S., Courbouleix, S., Lienhardt, M.-J., 1984. Synthèse géologique du Sud-Est de la France. Mémoire BRGM France, n° 125.

Delmas, M., 1965. Rapport de fin de sondage H.J. Essavilly 101. Société Nationale Pétrologique d'Aquitaine (S. N. P.A.).

Deville, E., 2021. Structure of the tectonic front of the Western Alps: Control of fluid pressure and halite occurrence on the decollement processes. Tectonics 1–21. https://doi.org/10.1029/2020TC006591

Deville, E., Blanc, E., Tardy, M., Beck, C., Cousin, M., Ménard, G., 1991. Thrust Propagation and Syntectonic Sedimentation in the Savoy Tertiary Molasse Basin (Alpine Foreland), in: Hydrocarbon and Petroleum Geology of France. Springer, pp. 269–280. https://doi.org/10.1007/978-3-642-78849-9_19

Dèzes, P., Schmid, S.M., Ziegler, P.A., 2004. Evolution of the European Cenozoic Rift System: interaction of the Alpine and Pyrenean orogens with their foreland lithosphere. Tectonophysics 389, 1–33. https://doi.org/10.1016/j.tecto.2004.06.011

Edel, J.B., Whitechurch, H., Diraison, M., 2006. Seismicity wedge beneath the Upper Rhine Graben due to backwards Alpine push? Tectonophysics 428, 49–64. https://doi.org/10.1016/j.tecto.2006.08.009

Egli, D., Mosar, J., Ibele, T., Madritsch, H., 2016. The role of precursory structures on Tertiary deformation in the Black Forest-Hegau region. Int. J. Earth Sci. 1–22. https://doi.org/10.1007/s00531-016-1427-8

Glangeaud, L., 1951. Interprétation tectono-physique des caractères structuraux et paléogéographiques de la Méditerranée occidentale. Bull. la Société Géologique Fr. 6, 735–762. https://doi.org/10.2113/gssgfbull.S6-I.8.735

Guellec, S., Mugnier, J.-L., Tardy, M., Roure, F., 1990. Neogene evolution of the western Alpine foreland in the light of ECORS data and balanced cross sections, in: Roure, F., Heitzmann, P., Polino, R. (Eds.), Deep Structures of the Alps. Mém. Soc. géol. suisse, pp. 165–185.

Hauber, L., 1993. Der südliche Rheingraben und seine geothermische Situation. Bull. der Vereinigung Schweizerischer Pet. und Ingenieure 60, 53–69. https://doi.org/10.5169/seals-216879

Homberg, C., Bergerat, F., Philippe, Y., Lacombe, O., Angelier, J., 2002. Structural inheritance and cenozoic stress fields in the Jura fold-and-thrust belt (France). Tectonophysics 357, 137–158. https://doi.org/10.1016/S0040-1951(02)00366-9

IGN-F, 2018. MNT RGE ALTI 5m, Digital Elevation Models. Institut national de l'information géographique et forestière (IGN-F).

Illies, H., 1962. Oberrheinisches Grundgebirge und Rheingraben. Geol. Rundschau 52, 317–332. https://doi.org/10.1007/BF01840083

Illies, J.H., 1972. The Rhine graben rift system-plate tectonics and transform faulting. Geophys. Surv. 1, 27–60. https://doi.org/10.1007/BF01449550

Jordan, P., 1992. Evidence for large-scale decoupling in the Triassic evaporites of northern Switzerland: an overview. Eclogae Geol. Helv. 85, 677–693. https://doi.org/10.5169/seals-167025

Jordan, P., Nuesch, R., 1989. Deformation Structures in the Muschelkalk Anhydrites of the Schafisheim Well (Jura Overthrust, Northern Switzerland). Eclogae Geol. Helv. 82, 429–454. https://doi.org/10.5169/seals-166384

King Hubbert, M., 1937. Theory of scale models as applied to the study of geologic structures. Bull. Geol. Soc. Am. 48, 1459–1520. https://doi.org/10.1130/GSAB-48-1459

Klinkmüller, M., Schreurs, G., Rosenau, M., Kemnitz, H., 2016. Properties of granular analogue model materials: A community wide survey. Tectonophysics 684, 23–38. https://doi.org/10.1016/j.tecto.2016.01.017

Lacombe, O., Bellahsen, N., 2016. Thick-skinned tectonics and basement-involved fold-thrust belts: insights from selected Cenozoic orogens. Geol. Mag. 153, 763–810. https://doi.org/10.1017/S0016756816000078

Larroque, J.M., Laurent, P., 1988. Evolution of the stress field pattern in the south of the Rhine Graben from the Eocene to the present. Tectonophysics 148, 41–58. https://doi.org/10.1016/0040-1951(88)90159-X

Laubscher, H., 2008a. 100 years Jura décollement hypothesis: How it affects Steinmann's (1892) 'Schwarzwaldlinie'. Int. J. Earth Sci. 97, 1231–1245. https://doi.org/10.1007/s00531-007-0224-9

Laubscher, H., 2008b. The Grenchenberg conundrum in the Swiss Jura: a case for the centenary of the thin-skin décollement nappe model (Buxtorf 1907). Swiss J. Geosci. 101, 41–60. https://doi.org/10.1007/s00015-008-1248-2

Laubscher, H.P., 1992. Jura kinematics and the Molasse Basin. Eclogae Geol. Helv. 85, 653–675. https://doi.org/10.5169/seals-167024

Laubscher, H.P., 1986. The eastern Jura: Relations between thin-skinned and basement tectonics, local and regional. Geol. Rundschau 75, 535–553. https://doi.org/10.1007/BF01820630

Laubscher, H.P., 1982. Die Südostecke des Rheingrabens - ein kinematisches und dynamisches Problem. Eclogae Geol. Helv. 75, 101–116. https://doi.org/10.5169/seals-165219

Laubscher, H.P., 1981. The 3D propagation of décollement in the Jura. Geol. Soc. Spec. Publ. 9, 311–318. https://doi.org/10.1144/GSL.SP.1981.009.01.27

Laubscher, H.P., 1965. Ein kinematisches Modell der Jurafaltung. Eclogae Geol. Helv. 58, 232–318. https://doi.org/10.5169/seals-163266

Laubscher, H.P., 1961. Die Fernschubhypothese der Jurafaltung. Eclogae Geol. Helv. 54, 222–282. https://doi.org/10.5169/seals-162820

Lefort, J.P., Agarwal, B.N.P., 1996. Gravity evidence for an Alpine buckling of the crust beneath the Paris Basin. Tectonophysics 258, 1–14. https://doi.org/10.1016/0040-1951(95)00148-4

Leloup, P.H., Arnaud, N., Sobel, E.R., Lacassin, R., 2005. Alpine thermal and structural evolution of the highest external crystalline massif: The Mont Blanc. Tectonics 24, 1–26. https://doi.org/10.1029/2004TC001676

Lienhardt, G., 1962. Géologie du bassin houiller stéphanien du Jura et de ses morts-terrains. Mémoires du Bur. Rech. Géologiques Miniéres N°9 449.

Lienhardt, M.-J., Aubague, M., Barféty, J.-C., Courel, L., Durand, M., Glintzboeckel, C., Mégard-Galli, J., 1984. Trias - Puissance et faciès de la partie supérieure, planche T2, in: Debrand-Passard, S., Courbouleix, S., Lienhardt, M.-J. (Eds.), Synthèse Géologique Du Sud-Est de La France, Mémoire Du BRGM N°126. BRGM France, p. T2.

Looser, N., Madritsch, H., Guillong, M., Laurent, O., Wohlwend, S., Bernasconi, S.M., 2020. Absolute Age and Temperature Constraints on Faulting along the Basal Décollement of the Jura Fold-and-thrust Belt from carbonate U-Pb Dating and Clumped Isotopes. Tectonics. https://doi.org/10.1002/Essoar.10503205.1

Lüthi, E., 1954. Geologische Untersuchungen im Gebiete zwischen Tessenberg und St.Immertal (Berner Jura). Promotionsarbeit Eidgenössische technische Hochschule Zürich, 9-37.

Madritsch, H., Deplazes, G., 2014. NTB 14-02, SGT Etappe 2: Vorschlag weiter zu untersuchender geologischer Standortgebiete mit zugehörigen Standortarealen für die Oberflächenanlage - Geologische Grundlagen - Dossier IV Geomechanische Unterlagen. Nationale Genossenschaft für die Lagerung radioaktiver Abfälle (Nagra), Wettingen, Switzerland.

Madritsch, H., Kounov, A., Schmid, S.M., Fabbri, O., 2009. Multiple fault reactivations within the intra-continental Rhine-Bresse Transfer Zone (La Serre Horst, eastern France). Tectonophysics 471, 297–318. https://doi.org/10.1016/j.tecto.2009.02.044

Madritsch, H., Naef, H., Meier, B., Franzke, H.J., Schreurs, G., 2018. Architecture and Kinematics of the Constance-Frick Trough (Northern Switzerland): Implications for the Formation of Post-Variscan Basins in the Foreland of the Alps and Scenarios of Their Neogene Reactivation. Tectonics 37, 2197–2220. https://doi.org/10.1029/2017TC004945

Madritsch, H., Schmid, S.M., Fabbri, O., 2008. Interactions between thin- and thick-skinned tectonics at the northwestern front of the Jura fold-and-thrust belt (eastern France). Tectonics 27. https://doi.org/10.1029/2008TC002282

Malz, A., Madritsch, H., Jordan, P., Meier, B., Kley, J., 2019. Along-strike variations in thin-skinned thrusting style controlled by pre-existing basement structure in the easternmost Jura Mountains (Northern Switzerland), in: Geological Society, London, Special Publications. Geological Society of London, pp. 199–220. https://doi.org/10.1144/SP490-2019-090

Malz, A., Madritsch, H., Meier, B., Kley, J., 2016. An unusual triangle zone in the external northern Alpine foreland (Switzerland): Structural inheritance, kinematics and implications for the development of the adjacent Jura fold-and-thrust belt. Tectonophysics 670, 127–143. https://doi.org/10.1016/j.tecto.2015.12.025

Martin, J., Mercier, É., 1996. Héritage distensif et structuration chevauchante dans une chaîne de couverture: apport de l'équilibrage par modélisation géométrique dans le Jura nord-occidental. Bull. la Soc. Geol. Fr. 167, 101–110.

Mary, B.C.L., Maillot, B., Leroy, Y.M., 2013. Deterministic chaos in frictional wedges revealed by convergence analysis. Int. J. Numer. Anal. Methods Geomech. 37, 3036–3051. https://doi.org/10.1002/nag.2177

Meier, B., 2010. NAB 10-40, Ergänzende Interpretation reflexionsseismischer Linien zwischen dem östlichen und westlichen Molassebecken: Gebiete Waadtland Nord, Fribourg, Berner Seeland und Jurasüdfuss zwischen Biel und Oensingen (Text und Beilage). Nationale Genossenschaft für die Lagerung radioaktiver Abfälle (Nagra), Wettingen, Switzerland.

Michel, P., Appert, G., Lavigne, J., Lefavrais, A., Donte, A., Liénhardt, G., Ricour, J., 1953. Le contact Jura-Bresse dans la région de Lons-le-Saunier. Bull. la Société géologique Fr. 6, 593–611. https://doi.org/10.2113/gssgfbull.s6-ii.7-8.593

Michon, L., 2000. Dynamique de l'extension continentale - Application au Rift Ouest-Européen par l ' étude de la province du Massif Central. Dr. thesis. Université Blaise Pascal.

Mosar, J., 1999. Present-day and future tectonic underplating in the western Swiss Alps: reconciliation of basement/wrench faulting and décollement folding of the Jura and Molasse basin in the Alpine foreland. Earth Planet. Sci. Lett. 173, 143–155. https://doi.org/10.1016/S0012-821X(99)00238-1

Müller, W.H., Schmid, S.M., Briegel, U., 1981. Deformation experiments on anhydrite rocks of different grain sizes: Rheology and microfabric. Tectonophysics 78, 527–543. https://doi.org/10.1016/0040-1951(81)90027-5

NASA, 2014. Shuttle Radar Topography Mission, 1-Arc Second scene. United States Geological Survey (USGS), College Park, Maryland.

Noack, T., 1995. Thrust development in the eastern Jura Mountains related to pre-existing extensional structures. Tectonophysics 252, 419–431. https://doi.org/10.1016/0040-1951(95)00089-5

Nussbaum, C., Kloppenburg, A., Caër, T., Bossart, P., 2017. Tectonic evolution around the Mont Terri rock laboratory, northwestern Swiss Jura: constraints from kinematic forward modelling. Swiss J.

Geosci. 110, 39–66. https://doi.org/10.1007/s00015-016-0248-x

Panien, M., Schreurs, G., Pfiffner, A., 2006. Mechanical behaviour of granular materials used in analogue modelling: insights from grain characterisation, ring-shear tests and analogue experiments. J. Struct. Geol. 28, 1710–1724. https://doi.org/10.1016/j.jsg.2006.05.004

Peper, T., Cloetingh, S., 1992. Lithosphere dynamics and tectono-stratigraphic evolution of the Mesozoic Betic rifted margin (southeastern Spain). Tectonophysics 203, 345–361. https://doi.org/10.1016/0040-1951(92)90231-T

Philippe, Y., 1995. Rampes latérales et zones de transfert dans les chaînes plissées: géométrie, conditions de formation et pièges structuraux associés. Université de Savoie. tel-00755680.

Philippe, Y., 1994. Transfer Zone in the Southern Jura Thrust Belt (Eastern France): Geometry, Development, and Comparison with Analogue Modeling Experiments, in: Mascle, A. (Ed.), Hydrocarbon and Petroleum Geology of France, Special Publication of the European Association of Petroleum Geoscientists. Springer Berlin Heidelberg, Berlin, Heidelberg, pp. 327–346. https://doi.org/10.1007/978-3-642-78849-9_23

Philippe, Y., Colletta, B., Deville, E., Mascle, A., 1996. The Jura fold-and-thrust belt: A kinematic model based on map-balancing., in: Ziegler, P.A., Horvàth, F. (Eds.), Peri-Tethys Memoir 2: Structure and Prospects of Alpine Basins and Forelands. Editions du Muséum Paris, pp. 235–261.

Ramberg, H., 1981. Gravity, Deformation and the Earth's Crust: in theory, experiments and geological applications. Academic Press, London.

Rat, P., 1974. Le système Bourgogne-Morvan-Bresse (articulation entre le bassin parisien et le domaine péri-alpin), in: Debelmas, J. (Ed.), Géologie de La France: Les Chaînes Plissées Du Cycle Alpin et Leur Avant-Pays. Doin, Paris, pp. 480–500.

Reisdorf, A.G., Wetzel, A., 2018. Evidence for synsedimentary differential tectonic movements in a low-subsidence setting: Early Jurassic in northwestern Switzerland. Swiss J. Geosci. 111, 417–444. https://doi.org/10.1007/s00015-018-0318-3

Rotstein, Y., Schaming, M., Rousse, S., 2005. Structure and Tertiary tectonic history of the Mulhouse High, Upper Rhine Graben: Block faulting modified by changes in the Alpine stress regime. Tectonics 24, 1–15. https://doi.org/10.1029/2004TC001654

Schardt, H., 1908. Les causes du plissement et des chevauchements dans le Jura. Eclogae Geol. Helv. 10, 484–488.

Schori, M., Mosar, J., Schreurs, G., 2015. Multiple detachments during thin-skinned deformation of the Swiss Central Jura: a kinematic model across the Chasseral. Swiss J. Geosci. 108, 327–343. https://doi.org/10.1007/s00015-015-0196-x

[dataset]Schori, M., Zwaan, F., Schreurs, G., Mosar, J., 2020. Supplementary material - Pre-existing

basement faults controlling deformation in the Jura Mountains fold-and-thrust belt: insights from analogue models. Mendeley Data V2. https://doi.org/10.17632/6pm5zwjv9w.2

Schreurs, G., Buiter, S.J.H., Boutelier, D., Corti, G., Costa, E., Cruden, A.R., Daniel, J.-M., Hoth, S., Koyi, H.A., Kukowski, N., Lohrmann, J., Ravaglia, A., Schlische, R.W., Withjack, M.O., Yamada, Y., Cavozzi, C., Del Ventisette, C., Brady, J.A.E., Hoffmann-Rothe, A., Mengus, J.-M., Montanari, D., Nilforoushan, F., 2006. Analogue benchmarks of shortening and extension experiments. Geol. Soc. London, Spec. Publ. 253, 1–27. https://doi.org/10.1144/GSL.SP.2006.253.01.01

Schumacher, M.E., 2002. Upper Rhine Graben: Role of preexisting structures during rift evolution. Tectonics 21, 6–17. https://doi.org/10.1029/2001TC900022

Sommaruga, A., 1997. Geology of the Central Jura and the Molasse Basin: new insight into an evaporite-based foreland fold and thrust belt. Mémoire la Société neuchâteloise des Sci. Nat. 12, 1–176.

Sommaruga, A., Eichenberger, U., Marillier, F., 2012. Seismic Atlas of the Swiss Molasse Basin, in: Kissling, E. (Ed.), Matériaux Pour La Géologie de La Suisse - Géophysique. Federal Office of Topography (swisstopo), p. 90.

Sommaruga, A., Mosar, J., Schori, M., Gruber, M., 2017. The Role of the Triassic Evaporites Underneath the North Alpine Foreland, in: Soto, J.I., Flinch, J., Tari, G. (Eds.), Permo-Triassic Salt Provinces of Europe, North Africa and the Atlantic Margins. Elsevier, pp. 447–466. https://doi.org/10.1016/b978-0-12-809417-4.00021-5

Stampfli, G.M., Mosar, J., Marquer, D., Marchant, R., Baudin, T., Borel, G., 1998. Subduction and obduction processes in the Swiss Alps. Tectonophysics 296, 159–204. https://doi.org/10.1016/S0040-1951(98)00142-5

Steinmann, G., 1902. Zur Tektonik des nordschweizerischen Kettenjura. Cent. für Mineral. Geol. und Paläontologie Stuttgart 483–492.

Steinmann, G., 1892. Bemerkungen über die tektonischen Beziehungen der oberrheinischen Tiefebene zu dem nordschweizerischen Kettenjura. Berichte der naturforschenden Gesellschaft zu Freibg. im Breisgbau 6, 150–159.

Strayer, L.M., Hudleston, P.J., Lorig, L.J., 2001. A numerical model of deformation and fluid-flow in an evolving thrust wedge. Tectonophysics 335, 121–145. https://doi.org/10.1016/S0040-1951(01)00052-X

Swisstopo, 2012. GeoCover geological vector data. Federal Office of Topography (swisstopo), Wabern, Switzerland.

Swisstopo, 2011. Digital elevation model swissALTI3D. Federal Office of Topography (swisstopo), Wabern, Switzerland.

Tavarnelli, E., 1997. Structural evolution of a foreland fold-and-thrust belt: The Umbria-Marche

Apennines, Italy. J. Struct. Geol. 19, 523–534. https://doi.org/10.1016/s0191-8141(96)00093-4

Trümpy, R., 1980. Geology of Switzerland a guide-book: An Outline of the Geology of Switzerland. Wepf & Co. Publishers, Basel - New York.

Tschanz, X., 1990. Analyse de la déformation du Jura central entre Neuchâtel (Suisse) et Besançon (France). Eclogae Geol. Helv. 83, 543–558. https://doi.org/10.5169/seals-166601

Ustaszewski, K., 2004. Reactivation of pre-existing crustal discontinuities: the southern Upper Rhine Graben and the northern Jura Mountains - a natural laboratory. Dr. thesis. University of Basel.

Ustaszewski, K., Schmid, S.M., 2007. Latest Pliocene to recent thick-skinned tectonics at the Upper Rhine Graben - Jura Mountains junction. Swiss J. Geosci. 100, 293–312. https://doi.org/10.1007/s00015-007-1226-0

Ustaszewski, K., Schmid, S.M., 2006. Control of preexisting faults on geometry and kinematics in the northernmost part of the Jura fold-and-thrust belt. Tectonics 25, 1–26. https://doi.org/10.1029/2005TC001915

Ustaszewski, K., Schumacher, M.E., Schmid, S.M., 2005. Simultaneous normal faulting and extensional flexuring during rifting: an example from the southernmost Upper Rhine Graben. Int. J. Earth Sci. 94, 680–696. https://doi.org/10.1007/s00531-004-0454-z

van Keken, P.E., Spiers, C.J., van den Berg, A.P., Muyzert, E.J., 1993. The effective viscosity of rocksalt: implementation of steady-state creep laws in numerical models of salt diapirism. Tectonophysics 225, 457–476. https://doi.org/10.1016/0040-1951(93)90310-G

Weijermars, R., Schmeling, H., 1986. Scaling of Newtonian and non-Newtonian fluid dynamics without inertia for quantitative modelling of rock flow due to gravity (including the concept of rheological similarity). Phys. Earth Planet. Inter. 43, 316–330. https://doi.org/10.1016/0031-9201(86)90021-X

Wetzel, A., Allenbach, R., Allia, V., 2003. Reactivated basement structures affecting the sedimentary facies in a tectonically 'quiescent' epicontinental basin: an example from NW Switzerland. Sediment. Geol. 157, 153–172. https://doi.org/10.1016/S0037-0738(02)00230-0

Winnock, E., 1961. Résultats géologiques du forage Risoux 1. Bull. der Vereinigung Schweizerischer Pet. und Ingenieure 28, 17–26. https://doi.org/10.5169/seals-191403

Withjack, M.O., Callaway, S., 2000. Active normal faulting beneath a salt layer: An experimental study of deformation patterns in the cover sequence. Am. Assoc. Pet. Geol. Bull. 84, 627–651. https://doi.org/10.1306/c9ebce73-1735-11d7-8645000102c1865d

Yang, K.M., Huang, S.T., Wu, J.C., Ting, H.H., Mei, W.W., 2006. Review and new insights on foreland tectonics in western Taiwan. Int. Geol. Rev. 48, 910–941. https://doi.org/10.2747/0020-6814.48.10.910

Yang, K.M., Wu, J.C., Wickham, J.S., Ting, H.H., Wang, J.B., Chi, W.R., 1996. Transverse structures

in Hsinchu and Miaoli areas: Structural mode and evolution in foothills belt, northwestern Taiwan. Pet. Geol. Taiwan 30, 111–150.

Ziegler, P.A., 1992. European Cenozoic rift system. Tectonophysics 208, 91–111. https://doi.org/10.1016/0040-1951(92)90338-7

Ziegler, P.A., 1988a. Evolution of the Arctic - North Atlantic and the Western Tethys - A Visual Presentation of a series of Paleogeographic-paleotectonic maps. AAPG Mem. 43, 164–196.

Ziegler, P.A., 1988b. Late Jurassic-Early Cretaceous Central Atlantic Sea-Floor Spreading, Closure of Neo-Tethys, and Opening of Canada Basin. AAPG Mem. Vol. 43 Evol. Arctic-North Atl. West. Tethys 63–82. https://doi.org/10.1306/M43478C6

Ziegler, P.A., Dèzes, P., 2007. Cenozoic uplift of Variscan Massifs in the Alpine foreland: Timing and controlling mechanisms. Glob. Planet. Change 58, 237–269. https://doi.org/10.1016/j.gloplacha.2006.12.004

Zwaan, F., Schreurs, G., Gentzmann, R., Warsitzka, M., Rosenau, M., 2018a. Ring-shear test data of quartz sand from the Tectonic Modelling Lab of the University of Bern (CH). GFZ Data Serv. 1–9. https://doi.org/10.5880/fidgeo.2018.028

Zwaan, F., Schreurs, G., Naliboff, J., Buiter, S.J.H., 2016. Insights into the effects of oblique extension on continental rift interaction from 3D analogue and numerical models. Tectonophysics 693, 239–260. https://doi.org/10.1016/j.tecto.2016.02.036

Zwaan, F., Schreurs, G., Ritter, M., Santimano, T., Rosenau, M., Naliboff, J., Buiter, S.J.H., 2018b. Rheology of PDMS-corundum sand mixtures from the Tectonic Modelling Lab of the University of Bern (CH). GFZ Data Serv. https://doi.org/10.5880/fidgeo.2018.023

Marc Schori: Conceptualization, Methodology, Validation, Formal analysis, Investigation, Data Curation, Writing – Original Draft, Writing - Review & Editing, Visualization **Frank Zwaan:** Conceptualization, Methodology, Writing - Review & Editing **Guido Schreurs:** Resources, Writing - Review & Editing, Supervision **Jon Mosar:** Resources, Writing - Review & Editing, Supervision, Funding acquisition

Declaration of interests

☒ The authors declare that they have no known competing financial interests or personal relationships that could have appeared to influence the work reported in this paper.

☐The authors declare the following financial interests/personal relationships which may be considered as potential competing interests:

- Brittle-viscous analogue models testing frontal and oblique fault-steps
- Basement faults controlling deformation of the Jura Mountains fold-and-thrust belt
- Rigid basement steps controlling viscous oblique-ramps
- Upward and downward steps localising deformation
- Rotation of step-controlled lineaments